Contour current driven continental slope-situated sandwaves with effects from secondary current processes on the Barents Sea margin offshore Norway

Edward L. King[1], Reidulv Bøe[2], Valérie K. Bellec[2], Leif Rise[2], Jofrid Skarðhamar[3], Bénédicte Ferré[4], Margaret Dolan[2]

[1]*Geological Survey of Canada-Atlantic (GSC-A), 1 Challenger Drive, P.O. Box 1006, Dartmouth, Nova Scotia, Canada B2Y 4A2, eking@nrcan.gc.ca*
[2]*Geological Survey of Norway (NGU), P.O. Box 6315 Sluppen, N-7491 Trondheim, Norway, Reidulv.Boe@ngu.no*
[3]*Institute of Marine Research (IMR), P.O. Box 6404, N-9294 Tromsø, Norway* jofrid.skardhamar@imr.no
[4]*CAGE—Centre for Arctic Gas Hydrate, Environment and Climate, Department of Geology, University of Tromsø (UiT), NO-9037 Tromsø, bfe000@post.uit.no*

Keywords: sandwave morphometrics, subaqueous dune, sand transport, Norwegian Atlantic Current, contour current, deep Ekman effect, internal wave,glacigenic debris flow

Abstract

Seabed data acquired from the southern Barents Sea continental margin offshore Norway reveal detailed morphology of large sandwave fields. Multibeam echosounder bathymetry and backscatter, shallow seismic, sediment samples and seabed video data collected by the MAREANO programme have been used to describe and interpret the morphology, distribution and transport of the sandwaves. The bedforms lie on a slope dominated by relict glacial forms and muddy/sandy/gravelly sediments. Sandwave migration across small gravity mass failures of the glacial mud constrains the fields initiation as early post glacial or later. The contour-parallel nature of the fields and crestlines normal to the bathymetry contours and the geostrophic Norwegian Atlantic Current (NwAC) demonstrate that the NNW- flowing oceanographic circulation is the primary driving current. The fields coincide with the depth range at which a transition between warm, saline and underlying cooler, less saline waters fluctuate across the seabed. Statistically rigorous measurements of height, width and various parameters of slope and symmetry confirm a tendency to downstream (NNW) sandwave migration but with significant exceptions. Anomalous bedform symmetry domains within the fields are tuned to meso-scale topography along (relict) glacial debris flow chutes, indicating current focusing. Upstream and upper slope-derived winnowed sand transport eroded from the glacial sediments is the supposed

source. Sandwave flank slope values are comparable to the regional slope such that the gravitational vector would have a cumulative downslope migration affect unless balanced by upslope drivers. Perpendicular cross-cutting of stoss face 3-D ripples by linear (2-D) ripples in the sandwave troughs and lee faces is evidence for non-synchronous, episodic current variations. Though deep Ekman transport and internal wave action is unproven here, these could explain chute-related tuning of bedform symmetry through funneling in the debris flow chutes and favor sand recycling, thus contributing to long-term maintenance of the sandwave field.

1. Introduction

The focus of this study are recently surveyed upper-slope situated sandwave fields in the SW Barents Sea of the Norwegian continental margin. Sandwaves are indicative of strong currents that potentially challenge water column and seabed engineering operations. Their dynamic nature poses challenges for seabed infrastructure such as pipelines and cables. While shelf-situated sandwaves are well documented on a global scale, the nearest located on the adjacent shelf (Bøe et al. 2009), known occurrences of present-day slope-situated sandwaves under a contour current influence are limited. These include examples on the Canary Islands (Wynn et al. 2000), the South China Sea (Damuth 1980; Reeder et al. 2011), the Strait of Gibraltar (Heezen and Hollister 1971), Gulf of Cadiz (Kenyon and Belderson 1973; Baraza et al. 1999; Habgood et al. 2003; Mulder 2003; Hanquiez et al. 2007), and the Faeroe–Shetland Channel (Masson 2001). Sandwaves in this study were first noted from sidescan investigations by Kenyon (1986) who attributed them to poleward current and suggested the potential of sand transport to the deep sea through associated channels.

Factors controlling deposition of continental shelf bottom-current sands (by tidal, wave and geostrophic currents) include hydrodynamic regime (seconds to years time scale), availability of sandy sediments (accumulation, export and preservation potential) and physiographic context of the area swept by the currents (Viana et al. 1998a ,1998b). All are modulated by a long-term (post-glacial) global sea-level and climate regime. The slope-setting processes affecting sandwaves are more poorly understood; those driven by contour currents are not well represented in the literature. A summary of deep-water sediment wave forms by Wynn and Stow (2002)

show dominance of those classified as “bottom current waves” and “turbidity current waves”. The former are generally associated with contouritic drifts, are generally larger, aligned oblique to the contours, muddy, bioturbated, and have long-term growth and transport histories. The latter are normally associated with turbidite channels and levees, often with crestlines parallel to contours, wavelengths changing downslope, and comprising a mix of turbidites and hemipelagic sediments. The Barents Sea sandwave fields contrast in a uniformly sand composition, constant contour-normal crestline orientation, relative independence of slope topographic perturbations and relatively short-lived (post-glacial) history.

Following the terminology of Belderson et al. (1982) we use the term sandwave to refer to the subaqueous, lower flow regime, transverse bedforms of sand that have wave lengths larger than sand ripples. Where two or more sizes of sandwaves occur together or superimposed it is convenient to refer to them as small sandwaves (identical to dunes or megaripples; see discussions in Allen 1980; Amos and King 1984; and Ashley 1990) and large sandwaves, without implying any genetic difference in the terminology. This is because there appears to be a complete gradation in size, plan view and lee slope angle between sandwaves at various locations (Belderson et al. 1982). In our study area the driving current is generally from SSE to NNW, along the Tromsøflaket slope, and the southern bedform face is referred to as stoss and the northern as lee except where noted.

The ultimate aim of the ongoing sandwave study is to elucidate governors of process, sand source, age of the bedform field and present mobility. Initial results of the sandwave study are reported in King et al. (2011). The focus here is to evaluate MAREANO’s (www.mareano.no) geological and geophysical data including multibeam bathymetry and backscatter, shallow seismic, videos and seabed samples, and initial oceanographic (conductivity, temperature, depth, CTD) measurements. We examine the general oceanographic setting, the geomorphology of features such as slope channels, slide scars and glacial debris flows within a sand sink-source context, make inferences from a rigorous dataset of measurements (metrics) on the bedforms, and synthesize these to suggest an origin and evolution of the sand and bedform fields and the processes driving their formation and mobility.

To date no detailed studies on the SW Barents Sea slope sandwave examples have been conducted. Several fields are present on the slope at a 600 to 800 m depth (Fig. 1). From the outset, the sandwave fields, lying in the path of the northern extension of the North Atlantic Current were recognized as probable manifestations of the geostrophic currents. Further study of the geologic setting and sandwave morphometric studies was undertaken to determine if secondary influence(s) on the sandwaves was revealed, such as topographic focusing, channeled up- or down welling, or internal waves. Furthermore, their spatial coincidence with an oceanographic thermocline positioned them as candidates for influence by (unproven) internal or solitary waves.

2. Bathymetric and Geologic Setting

The sandwave fields are located on the continental slope in the transition zone between the Norwegian Sea in the west and the Barents Sea in the east. The southern Barents Sea continental shelf comprises alternating shallow banks and deeper troughs formed during the last glaciations (Figs. 1 and 2), and massive diamictic sediments are found (Vorren et al. 1984; Ottesen et al., 2005; Andreassen et al. 2008; Winsborrow et al. 2010). The bank adjacent the sandwaves in the south, Tromsøflaket, is characterized by N-S-trending, very long and elevated moraines. The sandwave fields are only 1-3 kilometers from the 400 m deep shelf break off Tromsøflaket, but this increases to 6 km in the north.

The Bear Island Trough cuts across the Barents Sea shelf north of the sandwave area, with water depths of 300-400 m, transitioning to the Bear Island Trough Mouth Fan (Fig. 1) in the west (Laberg and Vorren 1995). At the shelf break, the 100 m high escarpments (Fig. 2) of the gigantic 200 000-300 000 years old Bear Island Slide occur (Laberg and Vorren 1993).

MAREANO data and data from earlier studies show a surficial sedimentation pattern on the continental shelf influenced by pre-existing glacial features and sediments, bathymetry and ocean currents (e.g., Hald and Vorren, 1984; Vorren et al. 1984, 1989; Bellec et al. 2008; Bøe et al. 2009, 2010; Buhl-Mortensen et al. 2010). Lag deposits occur on banks and locally on the

continental slope (Fig. 3), testifying to the influence of a high-energy environment eroding the glacial sediments. Deposition of fine-grained sediments occurs in troughs and sheltered depressions (Vorren et al. 1984; Michels 2000). The outermost shelf and just beyond the shelf break has little sand, with the exception of some partially filled iceberg scour troughs. Winnowing by along slope (contour) currents of the upper slope has occurred during interglacial periods (Laberg and Vorren 1993, 1995). A contourite deposit comprising fine-grained sediments has been described below 1000 m depth south of the study area, on the slope off Lofoten (Laberg et al. 1999; Laberg and Vorren 2004).

Glaciers advanced through fjords onto the continental shelf, locally developed into ice streams and reached the shelf edge during the last (late Weichselian) glaciation, which reached a maximum slightly before 18 000 C^{14} BP. Deglaciation of deep troughs took place from ~15 000 C^{14} BP, but ice was grounded on the outer shelf banks for a longer period (Winsborrow et al. 2010). During the middle-late Pleistocene, debris flow activity dominated the slope (Laberg and Vorren 1995; Vorren et al. 1998; Laberg et al. 2010). The debris flows have unique geometry, lithology and flow characteristics related to their shelf-break situated ice stream source and are termed glacigenic debris flows, abbreviated GDFs (King et al. 1996; Nygård et al. 2002).

In the northern part of the study area, seaward of the mouth of the Bear Island Trough, sub-bottom profiler data show that GDFs occur directly below the seabed sand unit (Fig. 4). These are characterized by a stacked, braided pattern with relief of only metres or less (Fig. 2). In the south they are blanketed with layered glacimarine deposits, locally up to a few metres thick, in turn covered with thin sand and gravel lags.

2.1 Gullies

There is a marked change from north to south in the presence of downslope channels or gullies with linear, dendritic and anastomosing patterns, both buried and surficial (Fig. 2 and 3). Gullies in the south are typically 20-40 m deep, while they may be up to 150 m deep lower on the slope, where they merge. The gully cuts have lens shaped infilling bodies with the acoustically semi-transparent, incoherent and homogeneous signal characteristic of GDFs (Laberg and Vorren 1995, Vorren et al. 1998; Laberg et al. 2010). They are interpreted to represent cohesive mass

transport, debris flow deposits derived from the flow processes inferred from the cited works and further refined from similar deposits on the North Sea Fan (Nygard et al. 2002). We interpret the gullies to be formed by debris flow activity (possibly initiated at sediment slide sites) emanating from the ice margin on Tromsøflaket and term them GDF chutes. The chutes are usually, but not exclusively, devoid of a capping glacimarine blanket (Figure 5, position a) in contrast to the more continuous blanket over GDFs outside the gullies. It is unclear if this represents GDF activity synchronous to the interfluve glacimarine blanket (and assimilation) or later (current) removal. The thalwegs are occasionally sandy at the immediate seabed, contrasting with ubiquitous gravel elsewhere.

Thus, cold and dense glacial margin-derived meltwater can have been instrumental in some of the chute history. Vorren et al. (1989) recognized these chutes (gullies) but attributed an interglacial cold (winter), dense shelf water and downslope transport process (cascading) on the basis that they are basically sediment-free (bypass sites). This is also the interpreted transport mechanism for long-term feeding of muddy contourites off the Spitsbergen margin (Rudels et al. 1999), but inferred during glacials. The 1989 work predated recognition of the GDF phenomenon and utilized low-resolution seismic, unable to resolve them in the partially filled gullies. The Spitsbergen work recognized intercalation of drift horizons and GDFs, much like observed here (Fig. 5, positions b and c). Cold and dense glacial margin-derived meltwater can have been instrumental in occasional removal or preventing deposition of the glacimarine blanket in the thalwegs. A limited post-glacial sandy downslope transport is considered in a later section (6.3).

Several large, submarine slides of poorly constrained age have occurred in the central and southern parts of the study area but are mainly covered by debris flow deposits and glacimarine sediments and present little seabed expression. Smaller slides with good seabed expression are scattered over the study area. At least 23 slides were identified within 10 km of the sandwave fields. These range from 0.5 to 4 km^2 and cut glacimarine sediments, post-dating the GDFs (Fig. 6).

The sands comprising the sandwaves lie on top of the GDFs or the glacimarine blanket (Fig. 7). They are invariably thin, the majority of sand within the sandwave itself, and it is common that the sandwave troughs coincide with the gravel lag marking the top of the glacigenic sediments.

3. Oceanographic Setting

The North Atlantic Current (NAC) (Norwegian Atlantic Current, NwAC along the Norwegian margin) carries warm and saline North Atlantic Water (NAW) into the Nordic Seas (Fig. 8). The NAC splits in two branches west of Tromsøflaket. One branch follows the continental slope north-northwestwards towards Svalbard, while one branch swings into the Barents Sea. The Norwegian Coastal Current also flows north, along the coast (Rudels et al. 1999).

Three well defined water masses are differentiated offshore Lofoten-Vesterålen-Troms along the NW Norwegian continental slope (e.g. Helland-Hansen and Nansen 1909; Hopkins 1991; Hansen and Østerhus, 2000). North Atlantic Water (NAW) is characterised by salinity > 35, and is typically found on the upper slope shallower than ca. 700 m depth. NAW has temperatures above 6º C at the mid-Norwegian margin (Haugan et al. 1991) and flows northeastwards along the slope with typical current speeds of 0.2-0.4 m/s (Heathershaw et al. 1998) but occasionally reaching surface velocities in excess of 1 m/s west of Lofoten and Vesterålen (Poulain et al., 1996). Norwegian Sea Arctic Intermediate Water (NSAIW) occurs at ca. 700-1000 m depth with temperatures between 0.5º C and -0.5º C and is less saline than the water masses above and below (Hansen and Østerhus, 2000). Norwegian Sea Deep Water (NSDW) occurs below ca. 1000 m with temperature below -0.5º C (Hansen and Østerhus, 2000). The depth of the transition zone between the water layers varies throughout the year, deepening in the winter, and long wavelength internal waves may occur.

4. Methods

The study area (Fig. 1) was mapped by multibeam echosounder (Kongsberg Simrad EM710, 70-100 kHz range) by the Norwegian Defence Research Establishment/Norwegian Mapping Authority in 2008-2009 as part of the MAREANO programme. The multibeam echosounder provides two datasets: bathymetry and backscatter. The backscatter (acoustic reflectance) is influenced mainly by sediment texture in the uppermost 0-30 cm of the seabed, and gives information on hardness and roughness. Backscatter data were processed via GRASS 5 software using beam correction and intensity normalization tools developed by the Geological Survey of Canada-Atlantic. Hard/rough bottoms (bedrock, coarse or compacted sediments) generally show higher backscatter values than soft/flat bottom (mud, uncompacted sediments). The data density was sufficient for gridding at 5 m, allowing detailed analysis of seabed features but no resolution of superimposed bedforms (seen in video coverage).

Sub-bottom profiling utilized a parametric sonar (TOPAS) from Kongsberg Maritime, a hull-mounted source centered on about 3.7 kHz, filtered and heave compensated. Vertical resolution exceeds 1 m and penetration is generally 20 to 30 m in the sand-covered glacial sediments.

A transect of conductivity, temperature, depth (CTD) casts was performed across the upper slope and shelf break near one of the sandwave fields on April 19th 2011 with R/V Helmer Hanssen. The DIVA Gridding method of the Ocean Data View software (Schlitzer, 2012) was used to interpolate the temperature and salinity data for identifying the water masses in the study area (Fig. 8).

Seabed sediment samples, video transects and the shallow seismic data were acquired during MAREANO cruises with the research vessel G.O. Sars in 2009-2010 to calibrate the multibeam backscatter data, and for biological, geological, and geochemical sampling and analysis. Sampling for biological and sedimentological studies was performed by grab, boxcorer, epibenthic sledge and beam trawl. The video surveys were performed using the Institute of Marine Research's towed video platform CAMPOD, which is a metal-framed tripod equipped with low light CCD overview camera and a high definition (HD) video camera. Further details on the CAMPOD and its operation are given in Bellec et al. (2008), Dolan et al. (2009) and Buhl-Mortensen et al. (2009).

4.1 Data processing and bedform analysis technique

The seismic data were interpreted using a publically available GSC desktop seismic software package (Courtney 2007) based on SEGY and efficient JPEG 2000 technology. For sand thickness distribution, horizon picks were readily exported as seabed to base of sand deposit to GIS (ESRI ArcMap 10) shapefiles.

Derivatives of the multibeam echosounder bathymetry grid included 3-D rendering, crestline tracing, seabed slope and statistically robust bedform metrics. Most analysis involved derivation of sandwaves morphometrics from the bathymetric grid to fully characterize the forms with a regional topography setting. The objective was to assemble a suite of derivative bedform metrics attributed to spatially preserved trough positions for viewing and statistical analysis in GIS. This was accomplished through a combination of extraction, filtering, auto-picking of troughs and crests and subsequent filtering in both ArcMap and spreadsheet (Excel) environments. Methods of bedform metrics extraction follow.

Six individual sandwave fields were outlined and designated north (N) and south (S) and numbered sequentially (N1-N5 and S1, Fig. 2). To sub-sample the 5 m gridded bathymetric digital elevation model, water depth profiles were extracted with elevation values for each 5 m along crestline-normal transects spaced at 100 m and fully covering each field. Eleven zones of such transects were generated (e.g. one for the S1 field, five for N2; a to e, etc.) to best align the profiles normal to the crestlines. There is sinuosity, of course, in the crestlines and accordingly some variation from the normal arose. This affects (slightly diminishes) true sandwave flank slope values (though ratios, such as asymmetry, remain valid). Deviation from the transect orientation was typically 10° to15° (one SD) relative to the transect. The extracted depth values (with associated UTM coordinates) along all such profiles were assembled in spreadsheets. An auto-picking routine was developed to recognize minima and maxima (troughs and crests). The profiles were smoothed slightly using a Hann filter to minimize small perturbations, presumably both noise and superimposed bedforms, whose measurement locally excluded recognition of the

larger (> 2 m high) bedforms in the auto-pick function. The auto-picked values were filtered to eliminate remnant low amplitude (<10 cm) and very short and long wavelength forms (10 m < λ >1000 m) which represented noise and small-scale glacigenic debris flow channel flanks respectively. Smoothing and metrics derivatives and definitions are shown graphically in Figure 9.

These measurements provided the basis for robust statistics of the bedform metrics, including height, wavelengths, profile symmetry, and stoss and lee flank slope, slope ratio and crest and trough sediment texture. All measurements (approximately 30 000 bedform profile samples) were assembled as GIS attributes (fields) for each data point trough location X-Y coordinate (UTM Zone 33) such that their spatial distributions within and among the fields could be investigated following re-entering the spreadsheet values in the GIS environment (Fig. 10).

4.2 Data Resolution and limitations

A small percentage of auto-pick "misses" relate to the larger bedforms (Fig. 10, open arrows in lower panel) either where they are compound (near crestline bifurcations) or have smaller, superimposed bedforms. This was deemed to occur so seldom as to have little statistical effect but it would skew the maxima slightly.

Although seabed video observations are not quantifiable in terms of bedform height, wavelength, slope, or compass orientation, the impression from derived photographs is that lee slopes are steeper than that measured from the multibeam. Slopes were measured from the extracted profiles (Fig. 9), generated at the same grid resolution as the multibeam grids such that values would match GIS-generated slope displays. Lee-slope crest to trough distances in video photographs appear to be several metres only; this is less than the 5 m gridding resolution of the multibeam which is constrained by acoustic spreading through the over 600 m water column. A 20º slope on a 2 m high hypothetical sandwave, for example, has a crest to trough distance close to the 5 m grid resolution and could be registered correctly if acoustic "pings" happen to be grid-sampled at the top and base of the lee slope. Yet the worst case scenario would yield a slope

measurement of only 7 º on such a bedform (mid stoss and mid lee ping samples). This situation worsens, of course, with slopes greater than 20 degrees. Only 0.1% of measured slopes exceed 20 degrees in this compilation. This does not necessarily negate the slope ratio index or the symmetry indices, which are relative measures, but it is clear that smoothing due to acoustic spreading sets serious limitations on small, angular seabed features such as observed in the video.

The outcome is that absolute slope and symmetry measurements (and their ratios) from the multibeam data represent “flatter” bedforms than in reality. The 5 m grid limitation has less serious implications for height and wavelength measures and their metrics derivatives but robust statistics should still yield significant and credible trends. Low resolution gridding has obvious implications for future serial surveys if migration rates are less than or close to 5 m between surveys.

5. Sandwaves and Sandwave Fields

5.1 Shape, Composition and Superimposed Ripples

Figure 11 shows a detailed example of the slope-situated sandwaves. These are small to mid-scale 2-dimensional with occasional bifurcations. They are generally largest in one or more centralized domains and diminish in height and wavelength toward the field boundaries. Some curvature of the crestlines is attributable to swings in the trends of underlying topography.

Orientation of the sandwave crestlines (Fig. 12) from manual traces of the multibeam image shows a strong SW-NE trend, normal to the trend of the local bathymetric contours. Crestline orientations are consistently normal to the regional slope ± 10° SD. Notably, crestline orientations are more tightly grouped than the bathymetric contours. Deviations of the contours from the NW-SE trend are related mainly to the meso-topography of slope-parallel glacigenic debris flow chutes. This illustrates a relative insensitivity of bedform orientation to these chutes as seen in Figures 2 and 11.

In profile, the sandwaves can be quite sinusoidal with symmetric or slightly asymmetric stoss-lee relationships as measured from the multibeam sonar grids but, as explained in section 4.2, this is a much smoothed dataset, not capable of resolving steep slopes. The video transects show a long stoss (southern) face with imperceptible slope (no slope or instrument orientation measurements were possible) and a very sharp crest line with a steep lee side oriented downstream, where possible to discern.

An overview of sediment composition is derived mainly from acoustic backscatter. The acoustic return from outer-beam transducers (those at low seabed incidence angle, outside about 20°), is sensitive to scattering, with stronger signal for rougher seabed. Gravel generally results in a stronger backscatter signal than sand and several 800 m long video transects across the bedforms confirm this (following paragraph). The data are plagued with noise (recognized in ship trackline patterns) but backscatter strength spans almost 50 db across the region and is generally about 10-20 db lower within the sandwave field than the surrounding gravel/cobble lag seabed. Sandwave troughs are frequently gravel floored where the sand thins sufficiently to expose a larger expanse of the basal gravel (Fig 11, panel B). Analysis (not shown here) demonstrates little or no net difference between crests and troughs on a whole field basis, partly because the troughs on the smaller, flanking sandwaves do not often reach down to the lag, and partly because the backscatter noise is often as strong as the crest-trough variation.

Seabed samples, though limited, confirm the seabed texture from acoustic backscatter. Grab samples (R571) from the southern S1 field, yielded gravel at a trough site and sand from a lee or stoss setting. A nearby box core recovered a few centimetres of well sorted sand and a multicorer (short gravity core-type carrousel) recovered 10-15 cm sand, grey on top transitioning to olive grey at 2 cm depth, with clear concentrations of the denser (dark coloured) minerals associated with ripples. These were sub-sampled (seven 1 cm thick slices) for further grain size analyses which yielded 100% fine to medium sand. The N2 field (R434) yielded small grab and box core samples of fine to medium sand, the former with traces of the coarse sand size shell hash which concentrates in the sandwave lee sides and ripple troughs. In the northern S1 sandwave field (R471, Fig. 3), grab and box core samples yielded up to 17.5 cm of fine sand.

A variety of ripples, superimposed on the sandwaves, are visible in the video-derived photographic stills. Figure 13 shows views of the lee edge of some sandwaves, emphasizing abrupt changes in superimposed ripple shape and crestline orientation. The sandwave crest and stoss typically have complex 3-D ripples (generally linguoid, panel A) with swirled patterns arising from sorting of shell hash and dark heavy minerals. Current sense from the strong asymmetry and ripple shape (A, C, and F) is, as expected, generally normal to the crestline trend of the sandwaves., No clear stoss- to lee-flank grain size difference is recognized.

A remarkable change in superimposed ripple type and orientation generally occurs at the sharp crest of the sandwave. Figure 13 (C, E, and F) shows three examples. The lee-face superimposed ripples are 2-D with very linear crests and occasional bifurcation. They are asymmetric and have crest orientations highly oblique to the sandwave crestline, occasionally almost normal. The contact between the two ripple types is abrupt with one “blending” to the other over less than 10 cm. The transition is a cross-cutting relationship where the newly-formed set appears to anchor to an existing crest, cannibalizing it. Clearly, shell-hash floored ripples at the base of the sandwave slip-face at Station 446 (Fig. 13, C and E) allow recognition of an asymmetry indicating transport direction to the photograph’s left. Comment marks behind trough-situated cobbles from other photographs (not shown) confirm this. We cannot be certain if this represents regional up-slope or down-slope ripple migration; the remote video Campod navigation was unreliable for much of the transect and the ROV did not have orientation sensors. However, profile asymmetry measurements from multibeam data (following section, 5.2) demonstrates that 85% of the sandwaves along this video transect display a neutral or NW-facing lee face (remainder to the SE). This indicates a good probability that these lee and trough-situated ripples demonstrate local upslope migration

In summary, sharp-crested sandwaves oriented slope-normal and with lee-face to the north are composed of fine to medium sand with shell hash, more prominent in the troughs. Some troughs bottom in a basal glacigenic gravel lag. Superimposed ripples are ubiquitous and periodically active. The abrupt contact in ripple type and orientation at the sandwave crest indicates that at least two different and successive current processes can be inferred, one a contour current and the other a regional up-slope (and possibly corresponding down-slope) component.

5.2 Sandwave Morphometrics

Sections 4.1 and 4.2 described derivation of sandwave metrics from multibeam sonar and their limitations. Various indices were generated to identify if morphology could point toward sediment processes. Results from this analysis are presented here. Table 1 summarizes field dimensions, height and wavelengths and symmetry. Table 2 summarizes bedform slopes, acoustic backscatter and sand source and sink volume estimates. Some of these parameters are also presented graphically in Figure 14. Figure 15 shows sandwave water depth, height and wavelength frequency distributions. The water depth mean at about 600 m (596±42, Fig. 15a) is spatially coincident the contact and depth range variation between NAW and NSAIW (Fig. 8).

Sandwave heights show a uniform exponential (normal) distribution with an average of 0.75 ±0.62 m (Fig. 15b). This is compatible with the video observations. Wavelengths (Fig. 15c) are similarly exponentially distributed (tail less than 30 m wavelength is likely due to limited sampling resolution). They are on average 39±16 m across with maxima in the 130 m range. Bedform size varies strongly within the field, mainly in an along-slope sense. Domains of the larger examples fall along the central axis of the sandwave fields but they also have some spatial affiliation with the larger changes in topography, generally near the flanks or on the interfluves of the GDF chutes/channels but this is not always the case.

The ratio of height to wavelength (H/L) is a common index of morphometrics and generally considered a rough proxy for bedform activity level (Flemming, 1980; Dyer 1986). Figure 16 shows this index for all fields, presented both as a height vs. wavelength plot (a) and as a frequency distribution of their ratio (b). The plot (a) has a columnar appearance due to the 5 m gridding of the original multibeam echosounder grid. Note that the bulk of measurements overlap in the lower left of the plot (the smaller forms) and their density is partially obscured. Dotted

lines mark the extremes at 5.5 m height and 210 m wavelength. Figure 16b shows the frequency distribution of H/L. Significance of the plots is considered below.

Bedform symmetry is a commonly used indicator of sandwave activity and direction of migration where long, low-sloped stoss (upstream) flanks combined with short, steep-sloped lee flanks yield highly asymmetric indices with clear mobility. Figure 17 shows summaries of symmetry and slope measurements. Despite many locations with examples to the contrary, Figure 17a shows that NW-facing slopes are marginally steeper than SE, considering the entire dataset. Together with the symmetry measurements showing the same, though slight trend, this is interpreted as a general northwesterly preferred migration direction.

Though bedform symmetry shows only weak overall trends where whole fields are considered, most fields exhibit geographic domains which are systematically spatially related to the topography of the GDF chutes. This also imparts a confidence in the asymmetry measurements, despite the shortcomings noted in section 4.2 because neither survey parameters, water column properties or processing procedures could create such trends related to the chutes. Figure 18 shows symmetry distribution across the N1 field (a) and two selected profiles (b) which accent the symmetry-skewness relation to the GDF chute flanks. The shaded relief image is optimized to highlight local slopes of the pre-existing GDF chutes and interfluves manifest as downhill-oriented banding demarcated with small, white arrows at the thalwegs. SE-facing slopes of the chutes have superimposed sandwaves with an asymmetry (skewness) in blue tones, indicative of up-hill migration in a downstream (NW) direction. However this pattern is mirrored in the NW slopes, where a green tone indicates up-hill skewness but inferred migration here is in an apparent *upstream* direction. This is manifest as banding in the blue and green dots (panel a) following the GDF chutes. The strongest trends are associated with the smaller bedforms flanking the field; the larger are more symmetric. Similar patterns (not illustrated) were found when NW to SE flank slope ratios were mapped, these emphasizing actual lee and stoss slope differences as opposed to the symmetry index.

Another aspect of symmetry was examined by comparing frequency distributions in the N1 field for a range in classified sandwave heights. The hypothesis was that large bedforms, with large

sand volumes, might have longer response time lags to variations in current direction than the smaller forms and thus better reflect an expected dominant long-term northeasterly flow direction. Figure 19 shows bedform size relationship to symmetry direction. Symmetry frequency distributions for five classes of bedform heights are compared. Median symmetry values are about +0.16 for all classes of bedform heights combined, compatible with the overall northwestward (general downstream) migration established earlier. The highest of bedforms (>1.5 m) display a much stronger asymmetry, most with northwestward (downstream) skew but with a clearly separate population displaying southeastward skew. The progressively lower height sandwaves, though still slightly skewed to downstream directions, include increasingly greater numbers of southeastward (upstream) skews. These observations suggest that rather than large bedforms showing a time-averaged northeasterly flow, as hypothesized, they preserve real and *opposite* yet relatively stable (long term) net current directions. Furthering this interpretation, the smaller forms likely react more quickly, reflecting variability of the current directions at their respective response capabilities.

6. Sandwave Field Formation and Maintenance: Sink, Source and Age

6.1 Sandwave Field Volume

The base of the sandwave sand was traced on all available TOPAS transects across the fields but distribution is inadequate for a complete sand volume assessment. Generally, troughs of the larger examples, centrally located in the fields, expose basal gravel lags while the flanks of the fields are continuous but thin (< 1 m) sand. Given inadequate seismic coverage, volume estimates were calculated based on sandwave half-height measurements. The latter were based on a simplified model of adjoining trochoidal shaped sandwaves whose troughs reach the underlying immobile gravel. Height and wavelength statistics from the 100m spaced transect profiles generated from the multibeam bathymetry were used to generate these volume estimates for each field (Sink Volume, Table 2). This technique suggests about 50 x 10^6 m^3 of sand in the S1 field, 15.7x10^6 m^3 in N2, and ranging from 0.1 to 3.9 for the other fields, for a total of about 72 x10^6 m^3 (0.07 km^3).

6.2 Sand Source from Winnowing

The only present day sand accumulation, apart from the sandwave fields, is extensive, irregular patches of sand and gravelly sand veneers over till on the shelf, (Fig. 3). These sands derive mainly from the sand component of the underlying glacigenic diamict through erosion by current winnowing as seen elsewhere (Vorren et al., 1984; Laberg et al. 1999; Laberg and Vorren 2004). There are no specific sand transport pathways to the slope evident in the present day sand distribution, except at the surface of the deeper part of GDF chutes but clearly the iceberg scoured, lag-covered till exposed here suffered winnowing and most of the fine sediment component was removed.

Above the shelf break this sand would have been largely till-derived but below the break the surficial sediment is primarily the GDFs and the stratified glacimarine sediments (Figs. 3, 4 and 5). These would be more subject to current erosion than the harder till but all varieties eventually develop a protective gravelly lag with only (early stage) iceberg scour turbation contributing "fresh" surfaces. Direct observation of winnowed lag is also clear in the seabed videos. Lag thickness is often limited to a mono-layer as evidenced by occasional fishing trawl cuts. An erosion thickness estimate from the sub-bottom profiler data is poorly constrained because amounts less than one metre would doubtfully be recognized in non-stratified sediments and would only be recognized in stratified sediments if it produced an angular unconformity rather than a disconformity. A winnowing source hypothesis for the sand seriously limits the volume of locally-generated sand.

6.3 Slope Bypass of Sand

The GDF chutes generally contain muddy mass transport deposits from glacial processes. How much post-glacial sand might they have directed to the base of slope? Data coverage at the base of slope is not available so identification of sandy lobes or sheets, if any, is not yet possible.

Though not measurable from sounder profiler, the acoustic backscatter proxy used for the surficial texture mapping in Figure 3, together with the video tracks, indicate a discontinuous, thin gravelly sand cover in the some thalwegs, often worked into ripples. The same phenomenon is observed at a smaller scale outside the chutes; linear trawl marks (scours from fishing activity in the area up to decimetres deep) observed on video have subsequently trapped sand. Thus, modern sand traction occurs, at least locally. It does not, however, confirm slope bypass; nor does it prove unidirectional transport.

The area of the N fields has a sand distribution restricted to the water depth range of the sandwave fields, ie. not preferentially along the chutes (Fig. 3). Also, the sandwave crestline patterns continue, apparently uninterrupted, across the chutes. This suggests that if any appreciable sand deposit has been captured (trapped) in the chutes, it is through a contour current process rather than via a down-slope conduit.

The northern third of the S1 field and immediately north is somewhat exceptional because here sand distribution is broader than the sandwave fields (Fig. 3). Here sand-filled iceberg scours extend to the shelf break and at least five sown-slope chute systems have significant, though generally not continuous bands of sand following their thalwegs. There is no clear spatial connection between shelf and slope sand bands but they are separated by only one to two km. If there is some chute-directed down-slope transport of sand, perhaps it is/was more active here but chute-directed slope-bypass of sand is not recognized as an important process compared to contour-directed transport.

6.4 Sand budget

In an attempt at establishing a sand budget for the winnowing hypothesis, estimates of erosion extent of the glacial muds and diamicts were calculated. The approach was to delineate areas of potential sand source up-slope of the individual sandwave fields and calculate erosion magnitude (thickness) necessary in order to balance with individual field sand volume estimates (Tables 1 and 2). These were based on assumed gravel and sand components of 5 and 25 percent respectively, typical for the parent glacigenic sediments. The sandwave formation process would

have further sorted the sands, probably removing some of the fine sand. Thus, current sorting of the parent diamict would reduce to a residual amount, matching the sandwave sand grain size, of only about 10%. Assuming a collection (source) area limited to the uppermost slope and this 10:1 reduction, requires vertical erosion of parent diamict between 50 and 150 cm for the northern fields (Table 2, second column from right). If the till area on the adjacent shelf is also added as potential winnowing source area, then winnowing thicknesses diminish to a 3 to 125 cm range (Table 2, right column) to balance with sand volume in the various fields. This invokes cross-shelf and downslope sand transport distances of typically 5 -10 km. The post-glacial eustatic lower-sea-level would have also acted to enhance shelf energy levels at that time. The greatest erosion estimate (125 cm) applies to the large S1 field but this value would diminish if we were to invoke a greater and more far-travelled component of contouritic (not downslope) sand source to this, the first (most upstream) in the string of fields. This erosion amount is sufficient to produce observed thin, protective lags given gravel clast content in the nearby parent sediments of from one to eight percent (presumably higher in the till).

6.5 Sandwave Field Age

In the Geologic Setting section the observation was made that the sandwaves not only transect the GDF chutes but also the mass failure scarps cut in glacimarine sediment overlying the debris flows. This places an early post-glacial maximum age on inception of the sandwaves. Slope-normal iceberg scours and long-transported ice rafted debris are early North Atlantic Drift indicators. The earliest inception would be when initial Atlantic water influx is recorded during the Bølling-Allerød interstadial (14.5 to 13.5 cal yr. B.P.) (Ślubowska-Woldengen et al. 2008), but they recognized stronger sub-surface inflow of saline water during the 9.5-7.5 cal yr. B.P. interval. If the sandwaves did not develop this early, then it probably was not until following the Neoglacial cooling (4.0-2.0 cal yr. B.P.) when fresh but sluggish circulation pertained (Slubowska-Woldengen et al. 2008). An early inception does not necessarily require a closed sand budget at the time; what sand volume might have passed downslope has left no geologic record.

7. Discussion

The slope setting the sandwave fields within the documented geostrophic contour current regime and the orientation of sandwave crests normal to the contours indicate a clear forcing of these sands by this geostrophic current. The CTD transect (Fig. 8) demonstrate the NAW and NSAIW water bodies and a spatial coincidence of the sandwave fields with the transition at the seabed. The transition depth between NAW and NSAIW has been observed to intersect the seabed between 600 and 400 m (Buhl-Mortensen et al. 2012; Ferré et al. 2012), connected to fluctuations in atmospheric forcing (Blindheim and Rey 2004), but with small mean seasonal changes (Mork and Skagseth 2010). Direct measurements at the site await analysis of results from recent deployments. The spatial coincidence of the bedform fields with a significant water column thermo-halocline intersection of the seabed raises the question of which secondary oceanographic processes might influence the sandwaves.

7.1 Sandwave Activity

These bedforms are mid-range in size within a global context (Amos and King 1984), the larger falling in the mid to large range. Generally, bedform size is positively related to current velocity (e.g. Rubin and McCulloch 1980) and there is generally a grain size dependency, with coarser sands supporting higher forms. Accordingly, the larger sandwaves likely mark the core of the driving geostrophic stream and smaller flanking forms reflect diminishing current magnitude. However, there are several documented cases where bedform field boundaries are due to increased velocities, not decreased, where sand becomes suspended instead of in traction, at least in fluvial/tidal examples. Other factors such as consolidation, lag deposits, and response time are also strong governors.

Small sandwaves tend to have a mean height/wavelength ratio of about 0.1 while that of active sandwaves is around 0.03, provided the sand source and development time is not limited (Dyer 1986). Figure 16b shows that examples above 0.03 are present but the bulk fall below this threshold. Flemming (1980) established another activity parameter based on height and

623 wavelength and these equations are shown graphically in Figure 16. Only about one quarter of
624 the sandwave points fall above the H_{mean} curve denoting active forms. The largest fields, N2 and
625 S1 contain proportionally many more active bedforms than other fields according to this criterion
626 (Fig. 16c). Curiously, the smallest N3 and N4 fields appear more active than the N1, exceptions
627 to a trend toward lower activity northward.
628
629 The video-observed ripples are clearly active, with sharp crests, asymmetries, and coarse troughs
630 Traction was observed during the 15 minute stationary portion of the R446 deployment. The
631 stoss-situated 3-D forms generate from stronger currents than the lee-situated straight-crested
632 examples. An active layer of centimeters to a decimetre is expected. The sharp cross-cutting of
633 these two forms at the sandwave crest is too sharp to represent sandwave morphology-induced
634 turbulence, directional spin or such reorganization of the currents. Rather it indicates non-
635 synchronous, periodic changes in flow from sandwave crestline normal to crestline parallel.
636 Lacking orientation of the video instrument restricts conclusions as to if this is up-slope or down-
637 slope transport (or both).
638
639 Thus, the H-L metrics alone suggest that some bedforms are active while many are relatively
640 moribund, with a greater proportion of active forms in the larger fields and a trend toward
641 diminished activity to the north. Superimposed ripples indicate current activity but by more than
642 one process; these are the mechanism by which the sandwaves are mobilized. The steep
643 sandwave lee slopes, not registered well from the sonar, further suggest a degree of activity.
644
645
646 *7.2 Sand recycling*
647
648 Inherent in a long-lived, closed but mobile sand system must be a mechanism for recycling most
649 of the sand within each field. The near-normal distribution of sandwave profile symmetry and
650 sandwave flanking slopes (Figs. 17 and 19) indicates mobility in both ‘upstream” and
651 “downstream” directions and provides at least the potential for recycling of sand. In order to
652 maintain the sand in a mid-slope setting, there must be an upslope component to the currents to
653 counter the gravitational component. Figure 20 shows a typical sandwave situation with

superimposed gravity vectors. Here, the regional downslope dip magnitudes nearly match stoss-, and to a lesser degree lee-face slopes. The implication is that the gravitational component must be significant, acting on sand grains approximately normal to the geostrophic current. Cumulative downslope components with each grain movement would eventually remove sand out of the system (down the slope) were it not for a counteracting force. Though some leakage in a "closed" sand budget is likely, we have argued that sand source has diminished as protective lags developed. The implication is that much of the sand is recycled within the fields. The lee and trough-situated 2-D ripples are an obvious candidate for transfer of sand up (or down) the regional slope. If, contrary to our arguments, the sand budget is not closed and/or if upstream and up-slope recycling is limited, this can only be reconciled with mobility of the sandwaves that is very slow but this contradicts most observations.

Establishing a sand budget potentially in balance only demonstrates that it is possible to generate and maintain the sands at this location on a long-term basis. It dictates a degree of sand mobility yet largely confined to field boundaries for long-term maintenance with a minimum flux of sand into and out of the field. Most observations are compatible with a dynamic system, more complex than simple feeding, bedform migration, and exiting of the sands from the fields. Of course, assumptions of sand source may be incorrect; present up-stream contour-current derived sand flux might be significant and sandwave migration proportionally active. Future work will address this.

7.3 Possible secondary oceanographic drivers: deep Ekman transport eddies and internal waves?

7.3.1 Long-term processes

Secondary processes inferred from the sandwave morphometrics are best related to relatively constant oceanographic processes with long term fluctuations or periodicities to which the inherently slow-responding large bedforms can tune. For instance, the meso-topographic-related domains in sandwave asymmetry (Figs. 18 and 19) representing components of current reversal, the requirement for long-term sand recycling, and the inferred up-slope sand transport component (from ripples) might be explained by the cumulative and/or combined effect of such processes, even if episodic. Potential influencing processes could be seasonal (winter)

685 downwelling (as suggested in Rebesco et al. 2013), seasonal eddies, meandering of the isobath
686 current, or deep Ekman rotation. Some elaboration follows.
687
688 Slope-situated topographic perturbations, such as the GDF chutes, would have similar cross-
689 isobath effects on currents as those produced by small canyons, depending on their size.
690 Modeling of canyon-effect in some settings (e.g. Allen 2004; Lima et al. 2007) can yield up- and
691 down-welling and eddies so strong as to mask the isobath current. Geostrophic currents (as
692 opposed to wind) can induce deep Ekman transport to the left (thus downslope, here) in the
693 bottom boundary layer (e.g. Cushman-Roisin 1994; Taylor and Sarkar 2008). Heathershaw et al.
694 (1998) inferred deep anti-cyclonic rotation through the Ekman effect from a mooring transect
695 across the slope to the south, off Vestfjorden. This may explain down-slope migrating sand
696 waves/ripples of vertical scales smaller than the bottom boundary layer thickness. Beyond this,
697 temporal variability in both currents and vertical stratification of the water masses driven by
698 different oceanographic mechanisms will influence the sandwaves in different seasons (e.g.
699 Ramsden 1995; Brink and Lentz 2010). The combined vectors over long (seasonal?) timespans
700 might, however, be sufficient to generate sandwave migration trends deviating from a simple
701 northwesterly direction. The seabed effect of these may also migrate with long-term up- and
702 down-slope movement of the stratified cold to warm transition.
703
704
705 7.3.2 Short-term processes
706 The strongest evidence for secondary current process is the very sharp crosscutting observation
707 of the 2-D lee-face ripples on the stoss-situated 3-D ripples (Fig. 13); each set formed at a
708 different time and at directions normal to the primary current. Any explanation need only invoke
709 a short-term hydrologic process, as outlined below, given the short response time for ripples. A
710 similar phenomenon, but on the shelf to the south had clear secondary tidal current influence
711 (Bøe et al. 2009).
712
713 The effects of tide on sediment transport are not generally considered strong at great water
714 depths but the cross-cutting ripple fields require a frequent, strong and temporally direction-
715 changing driver. A slope to shelf mooring transect located to the south (off Vestfjorden,

716 Heathershaw et al. 1998) demonstrated observations, consistent with models, indicating strong
717 enhancements of K_2 and M_2 (diurnal and semi-diurnal) currents within the isobaths current at
718 depths similar to the Barents Sea sandwave fields. However, the magnitude of such secondary
719 processes to the main geostrophic current at water depths over 700 m are not expected, acting on
720 their own, to be sufficient for sand traction. Heathershaw et al. 1998 could not demonstrate
721 internal tide-generated waves; neither have they yet been empirically demonstrated nor modelled
722 in the area. However, the warm, mixed upper slope water and cool, less saline underlying water
723 creates a potential interface for reflection of such waves to the seabed. This process can produce
724 sufficient turbulent energy dissipation for sediment non-deposition, entrainment and erosion (e.g.
725 Cacchione, et al. 2002; Puig, et al. 2004), including sandwave formation (Karl et al. 1986;
726 Reeder et al. 2011). The Reeder et al. (2011) study suggests a strong influence for large
727 sandwaves (up to 16 m amplitude) in the China Sea where exceptionally powerful tidally forced
728 internal solitary waves impact the slope. The high frequency-short duration, high energy and
729 potential for both up- and down-slope sediment mobility properties of internal waves is
730 compatible with the interruption and overprinting of the geostrophic current as indicated by the
731 cross-cutting ripple patterns. The studies cited here include end-member situations; the
732 magnitude of these processes, if indeed they are extant for the Barents Sea examples, could be
733 diminished in relation to the primary geostrophic current.
734
735
736 **8. Summary and Conclusions**
737
738 Slope-situated, channelized GDFs derived from an ice sheet at the shelf break during the last
739 glacial maximum and syn-depositional glacimarine muds with thin, winnowed, gravelly sand lag
740 are locally overlain by thin sand bodies worked into sandwaves. Sandwave fields at between 500
741 and 700 m water depth range in width from 0.4 to 3.5 km and length from 1.6 to 36 km, totaling
742 130 km^2. Crestline orientations are consistently normal to the regional slope. These average
743 0.7±0.6 m (maximum 5.5 m) height and 58±24 m (maximum 205 m) wavelength, comprising
744 fine to medium, well sorted sand. There is no stratigraphy or preservation of earlier sandwaves.
745 The hemipelagic sediments failed locally as small rotational and translation slides but the
746 sandwaves cross these, unaffected morphologically. Failures had to be post-glacial (after ca. 15

747 ka), broadly constraining sandwave field initiation. However, timing and magnitude of paleo-
748 current evolution in early post-glacial times and, by proxy, the initiation and duration of
749 sandwave activity is poorly constrained.
750
751 Volume considerations and lack of evidence for extensive downslope sand transport from the
752 Barents Sea shelf suggest the sand source is local (within tens of km), derived from current
753 winnowing of the uppermost glacial sediments distributed across the upper slope and outer shelf,
754 leaving a lag on the muddy diamicts. A crude sand budget suggests a closed system whereby the
755 sediment sink is largely within the sandwave bodies themselves.
756
757 A robust morphometric cataloguing of the bedforms allowed statistical presentations of several
758 indices which suggest at least periodic mobility in at least sub-field domains of the bedforms.
759 Height-wavelength ratios suggest up to 25% of the forms are active but insufficient sonar
760 resolution tends to underestimate this. An active layer on the sandwaves demonstrated by current
761 ripples includes starkly contrasting types and direction at the sharp sandwave crestline indicating
762 a short-term up-and/or downwelling process. Tendency toward the expected net down-current
763 (northwestward, contour-parallel) migration is demonstrated by bedform symmetry and stoss-lee
764 slope differences but trends in the opposite direction nearly balance this. Long-term mobility of
765 the larger bedforms must be inferred from their morphology until serial re-surveying is
766 conducted.
767
768 There is an expression of local hydrologic steering in a tuning of bedform symmetry to the meso-
769 morphology of the slope-parallel GDF chutes. Bedform asymmetries suggest up-hill migration
770 on both “upstream” and “downstream” flanks with respect to a northwestward flowing contour
771 current. Furthermore, an upslope driving hydrologic component (normal to regional contours) is
772 inferred to counter tendencies of gravity-driven grain migration.
773
774 A combination of inferred secondary currents, both arising from the stable or recurring eddies,
775 deep Ekman transport can contribute to both maintenance of sand within the fields on the mid-
776 slope and to asymmetries through steering across GDF chute flanks. Tidal-driven internal waves
777 along the transition between NSAIW and NAW, though not directly observed are a mechanism

which could impact the slope at the sandwave field depth with sufficient energy and frequency to entrain sand in ripples. The spatial coincidence of the fields with the water mass interface, the seasonal migration of this zone across the full water depth range of the field, and an analogy with the demonstrated link between internal waves and slope-situated sandwaves in the China Sea all suggest an influence of these processes on the sandwave fields.

The relative impact of the oceanographic current and secondary processes remains to be answered through more detailed field study of the oceanography, sand stratigraphy and mid-term bedform mobility. Current measurements and high resolution numerical modeling experiments are planned to observe secondary oceanographic phenomena and to investigate topographic effects at the appropriate scale for explaining some of the sandwave morphological perturbations. Further, high resolution acoustic surveying to better map sand thickness, sampling for sedimentological analyses, and serial multibeam surveying to observe direct changes in sandwave patterns are planned.

Acknowledgments

The MAREANO programme and the Norwegian Deepwater Programme (NDP) are thanked for data and financial support to publish this paper. The first author's participation in the project was under NGU auspices while on leave from the Geological Survey of Canada. The GSC subsequently provided latitude for manuscript preparation in support of related goals on the Canadian margin. Benedicte Ferre is affiliated with the Centre of Excellence: Arctic Gas hydrate, Environment and Climate (CAGE) funded by the Norwegian Research Council (grant no. 223259). Michael Li, GSC-Atlantic, provided initial review. Jan Sverre Laberg, University of Tromsø and Adriano Viana, Petrobras kindly contributed to a better focus on the processes, manuscript clarity and attention to details with their reviews.

References

Allen, S.E., 2004. Restrictions on deep flow across the shelf-break and the role of submarine canyons in facilitating such flow. Surveys in Geophysics 25, 221-247.

Allen, J.R.L., 1980. Sand waves: a model of origin and internal structure. Sedimentary Geology 26, 281-328.

Amos, C.L., King, E.L., 1984. Bedforms of the Canadian eastern seaboard: a comparison with global occurrences. Marine Geology 57, 167-208.

Andreassen, K., Laberg, J.S., Vorren, T.O. 2008. Seafloor geomorphology of the SW Barents Sea and its glaci-dynamic implications. Geomorphology 97, 157-177.

Ashley, G.M., 1990. Classification of large-scale subaqueous bedforms: a new look at an old problem. Journal of Sedimentary Research 60, 161-172.

Baraza, J., Ercilla, G., Nelson, C.H., 1999. Potential geological hazards on the eastern Gulf of Cadiz slope (SW Spain). Marine Geology 155, 191-215.

Belderson, R.H., Johnson, M.A. Kenyon, N.H., 1982. Bedforms, in: Stride, A.H. (Ed.), Offshore Tidal Sands: Processes and Deposits. Chapman & Hall, London, pp.27-57.

Bellec, V.K., Wilson, M., Bøe, R., Rise, L., Thorsnes, T., Buhl-Mortensen, L., Buhl-Mortensen, P., 2008. Bottom currents interpreted from iceberg ploughmarks revealed by multibeam data at Tromsøflaket, Barents Sea. Marine Geology 249, 257-270.

Bellec, V. K., Van Lancker, V. R. M., Degrendele, K., Roche, M., Le Bot, S., 2010. Geo-environmental characterization of the Kwinte Bank (North Sea). Journal of Coastal Research, Special issue 51, 63-76.

838 Bellec, V., Picard, K., Bøe, R., Thorsnes, T., Rise, L., Dolan, M., Elvenes, S., Lepland, A.,
839 Hansen, O.H., 2012a. Geologisk havbunnskart, Kart 71301600, September 2012. M 1: 100 000.
840 Norges geologiske undersøkelse.
841
842 Bellec, V., Picard, K., Bøe, R., Thorsnes, T., Rise, L., Dolan, M., Elvenes, S., Lepland, A.,
843 Hansen, O.H., 2012b. Geologisk havbunnskart, Kart 71001600, September 2012. M 1: 100 000.
844 Norges geologiske undersøkelse.
845 (These two Bellec et al. surficial geology 1:100 000 scale maps available at:
846 http://www.ngu.no/no/hm/Kart-og-data/Maringeologiske-kart/havbunn-nedlasting/#Ferdige)
847
848 Blindheim, J., Rey, F. 2004. Water-mass formation and distributions in the Nordic Seas during
849 the 1990s. ICES Journal of Marine Science, 61: 846-863.
850
851 Buhl-Mortensen P.B., Buhl-Mortensen, L., Dolan, M., Dannheim, J., Kröger, K., 2009.
852 Megafaunal diversity associated with marine landscapes of northern Norway: a preliminary
853 assessment. Norwegian Journal of Geology 89, 163-171.
854
855 Buhl-Mortensen, L., Hodnesdal, H., Thorsnes, T. (Eds.) 2010. Til bunns i Barentshavet og
856 havområdene utenfor Lofoten - ny kunnskap fra MAREANO for økosystembasert forvaltning.
857 Norges Geologiske Undersøkelse, Trondheim, Norway. 128 pp. (English summary).
858
859 Buhl-Mortensen, L., Bøe, R., Dolan, M. F. J., Buhl-Mortensen, P.B., Thorsnes, T., Elvenes, S.,
860 Hodnesdal, H. 2012. 51 - Banks, Troughs, and Canyons on the Continental Margin off Lofoten,
861 Vesterålen, and Troms, Norway, in: T. H. Peter and K. B. Elaine (Eds.). Seafloor
862 Geomorphology as Benthic Habitat, Elsevier, London, pp. 703-715.
863
864 Bøe, R., Bellec, V.K., Dolan, M.F.J., Buhl-Mortensen, P.B., Buhl-Mortensen, L., Rise, L., 2009.
865 Giant sand waves in the Hola glacial trough off Vesterålen, North Norway. Marine Geology 267,
866 36-54.
867

Bøe, R. Bellec, V. Thorsnes, T. Picard, K, Dolan, M., Rise, L., 2010. Tromsøflaket og Eggakanten, p. 27-35. in: Buhl-Mortensen, L., Hodnesdal, H., Thorsnes, T. (Eds.) Til bunns i Barentshavet og havområdene utenfor Lofoten - ny kunnskap fra MAREANO for økosystembasert forvaltning. Norges Geologiske Undersøkelse, Trondheim, Norway. 128 pp. (English summary).

Brink, K. H. , Lentz, S. J. 2010. Buoyancy arrest and bottom Ekman transport. Part II: Oscillating flow. Journal of Physical Oceanography 40, 636-655.

Cacchione, D.A., Pratson, L.F., Ogston, A.S., 2002. The Shaping of Continental Slopes by Internal Tides. Science 296, 724-727.

Courtney, R., 2007. Storage and Dissemination of SEGY Data in JPEG2000 Format. American Geophysical Union, Fall Meeting abstract #IN51B-0402.

Cushman-Roisin, B. 1994. Introduction to geophysical fluid dynamics. Englewood Cliffs, N.J., Prentice Hall.

Damuth, J.E., 1980. Use of high-frequency (3.5–12 kHz) echograms in the study of near-bottom sedimentation processes in the deep-sea: A review. Marine Geology 38, 51-75.

Dolan, M., Mortensen, P.B., Thorsnes, T., Buhl-Mortensen, L., Bellec, V.K., Bøe, R., 2009. Developing seabed nature-type maps offshore Norway: initial results from the MAREANO programme. Norwegian Journal of Geology 89, 17-28.

Dyer, K.R., 1986: Coastal and estuarine sediment dynamics. Wiley & Sons, Chichester, England.

Ferré, B., Mienert, J. , Feseker, T., 2012. Ocean temperature variability for the past 60 years on the Norwegian-Svalbard margin influences gas hydrate stability on human time scales. Journal of Geophysical Research 117, C10017.

898 Flemming, B.W. 1980. Sand transport and bedform patterns on the continental shelf between
899 Durban and Port Elizabeth (southeast African continental margin). Sedimentary Geology 26,
900 179-205.
901
902 Habgood, E.L., Kenyon, N.H., Masson, D.G., Akhmetzhanov, A., Weaver, P.P.E., Gardner, J.,
903 Mulder, T., 2003. Deep-water sediment wave fields, bottom current sand channels and gravity
904 flow channel-lobe systems: Gulf of Cadiz, NE Atlantic. Sedimentology 50, 483-510.
905 Hald, M., Vorren, T.O., 1984. Modern and Holocene foraminifera and sediments on the
906 continental shelf off Troms, North Norway. Boreas 13, 133-154.
907
908 Hansen, B., Østerhus, S., 2000. North Atlantic-Nordic Seas exchanges, Progress In
909 Oceanography 45, 2, 109-208.
910
911 Hanquiez, V., Mulder, T., Lecroart, P., Gonthier, E., Marchès, E., Voisset, M., 2007. High
912 resolution seafloor images in the Gulf of Cadiz, Iberian margin. Marine Geology 246, 42-59.
913
914 Haugan, P. M., Evensen, G., Johannessen, J. A., Johannessen, O. M., Pettersson L. H., 1991.
915 Modeled and Observed Mesoscale Circulation and Wave-Current Refraction During the 1988
916 Norwegian Continental Shelf Experiment. Journal of Geophysical Research 96(C6), 10487-
917 10506.
918
919 Heathershaw, A. D., P. Hall, J. M. Huthnance. 1998. Measurements of the slope current, tidal
920 characteristics and variability west of Vestfjorden, Norway. Continental Shelf Research 18,
921 1419-1453.
922
923 Helland-Hansen, B., Nansen F. 1909. The Norwegian sea : its physical oceanography based upon
924 Norwegian researches 1900-1904, Report on Norwegian Fishery and Marine investigations Vol.
925 II 1909 Mo. 2. 390 pp., Det Mallingske bogtrykkeri, Kristiania.
926
927 Heezen, B.C., Hollister, C.D., 1971. The face of the deep. Oxford University Press, New York.
928

929 Hopkins, T.S. 1991. The GIN Sea—A synthesis of its physical oceanography and literature
930 review 1972–1985. Earth-Science Reviews 30, 175-318.
931
932 Karl, H.A., Cacchione, D.A., Carlson, P. R., 1986. Internal-wave currents as a mechanism to
933 account for large sand waves in Navarinsky Canyon Head, Bering Sea. Journal of Sedimentary
934 Petrology 56, 706-714.
935
936 Kenyon, N.H., 1986: Evidence from bedforms for a strong poleward current along the upper
937 continental slope of northwest Europe. Marine Geology 72, 186-198.
938
939 Kenyon, N.H., Belderson, R.H., 1973. Bedforms of the Mediterranean undercurrent observed
940 with sidescan sonar. Sedimentary Geology 9, 77-99.
941
942 King, E.L., Bøe, R., Bellec, V.K., Rise, L. Dolan, M., 2011. Contour current driven sandwaves
943 on the upper slope of the continental margin offshore northern Norway - setting and
944 morphometrics. NGU Report 2011.073, 93 p.
945
946 King, E.L., Sejrup, H.P., Haflidason, H., Elverhøi, A., Aarseth, I., 1996. Quaternary Seismic
947 Stratigraphy of the North Sea Fan: Glacially-fed Gravity Flow Aprons, Hemipelagic Sediments,
948 and Large Submarine Slides. Marine Geology 130, 293-315.
949
950 Laberg, J.S., Vorren, T.O., 1993. A Late Pleistocene submarine slide on the Bear Island Trough
951 Mouth Fan. Geo-Marine Letters 13, 227-234.
952
953 Laberg, J.S., Vorren, T.O., 1995. Late Weichselian submarine debris flow deposits on the Bear
954 Island Trough Mouth Fan. Marine Geology 127, 45-72.
955
956 Laberg, J.S., Vorren, T.O., Knutsen, S.M., 1999. The Lofoten contourite drift off Norway.
957 Marine Geology 159, 1-6.
958

Laberg, J.S., Vorren, T.O., 2004. Weichselian and Holocene growth of the northern high-latitude Lofoten Contourite Drift on the continental slope of Norway. Sedimentary Geology 164, 1-17.

Laberg, J.S., Andreassen, K., Knies, J., Vorren, T.O., Winsborrow, M., 2010. Late Pliocene-Pleistocene development of the Barents Sea Ice Sheet. Geology 38/2, 107-110.

Lima, J.A.M., Möller, O.O., Viana, A.R., & Piovesan, R., 2007. Hydrodynamic modelling of bottom currents and sediment transport in the Canyon São Tomé (Brazil). in: Viana, A. R. & Rebesco, M. (Eds.) Economic and Palaeoceanographic Significance of Contourite Deposits. Geological Society, London, Special Publications, 276, 329-342.

Masson, D.G., 2001. Sedimentary processes shaping the eastern slope of the Faeroe–Shetland Channel, Continental Shelf Research 21, 825-857.

Michels, K.H., 2000. Inferring maximum geostrophic current velocities in the Norwegian-Greenland Sea from measurements of sediment surface samples: methods, application, and results. J. Sediment. Res. 70, 1036-1050.

Mork, K. A., Skagseth, O. 2010. A quantitative description of the Norwegian Atlantic Current by combining altimetry and hydrography. Ocean Science 6(4), 901-911.

Mulder, T., 2003. Deep-water sediment wave fields, bottom current sand channels and gravity flow channel-lobe systems: Gulf of Cadiz, NE Atlantic. Sedimentology 50, 483-510.

Nygård, A., Sejrup, H.P., Haflidason, H., King, E.L., 2002. Geometry and genesis of glacigenic debris flows on the North Sea Fan: TOBI imagery and deep-tow boomer evidence, Marine Geology 188, 15-33.

Ottesen, D., Dowdeswell, J.A., Rise, L., 2005. Submarine landforms and the reconstruction of fast-flowing ice streams within a large Quaternary ice sheet: the 2,500 km-long Norwegian–Svalbard margin (57°-80° N). Geological Society of America Bulletin 117, 1033-1050.

991 Poulain, P.-M., Warn-Varnas, A., Niiler, P. P., 1996. Near-surface circulation of the Nordic seas
992 as measured by Lagrangian drifters. Journal of Geophysical Research 101, 237-258.
993
994 Puig, P., Palanques, A., Guillén, J., El Khatab, M., 2004. Role of internal waves in the generation
995 of nepheloid layers on the northwestern Alboran slope: Implications for continental margin
996 shaping. Journal of Geophysical Research 109, C09011.
997
998 Ramsden, D. 1995. Response of an oceanic bottom boundary-layer on a slope to interior flow .1.
999 Time-independent interior flow. Journal of Physical Oceanography 25, 1672-1687.
1000
1001 Rebesco, M., Wåhlin, A., Laberg, J.S., Schauer, U., Beszczynska-Möller, A., Lucchi, R.G.,
1002 Noormets, R., Accettella, D., Zarayskaya, Y., Diviacco, P. 2013. Quaternary contourite drifts of
1003 the Western Spitsbergen margin. Deep-Sea Research I, 156-168.
1004
1005 Reeder, D.B., Ma, B.B., Yang, Y.J., 2011. Very large subaqueous sand dunes on the upper
1006 continental slope in the South China Sea generated by episodic, shoaling deep-water internal
1007 solitary waves. Marine Geology 279, 12-18.
1008
1009 Rudels, B., H. J. Friedrich, D. Quadfasel. 1999. The Arctic Circumpolar Boundary Current, Deep
1010 Sea Research Part II: Topical Studies in Oceanography, 46(6–7), 1023-1062,
1011
1012 Rubin, D.M., McCulloch, D.S., 1980. Single and superimposed bedforms: a synthesis of San
1013 Francisco Bay and flume observations. Sedimentary Geology 26, 207-231.
1014
1015 Schlitzer, R., 2012. Ocean Data View, http://odv.awi.de
1016
1017 Ślubowska-Woldengen, M., Koç, N., Rasmussen, T.L., Klitgaard-Kristensen, D., Hald, M.,
1018 Jennings, A.E., 2008. Time-slice reconstructions of ocean circulation changes on the continental
1019 shelf in the Nordic and Barents Seas during the last 16,000 cal yr BP. Quaternary Science
1020 Reviews 27, 1476-1492.
1021

Taylor, J.R., Sarkar, S. 2008. Stratification effects in a bottom Ekman layer. Journal of Physical Oceanography 38, 2535-2555.

Viana, A.R., Faugères, J.-C., Stow, D.A.W., 1998a. Bottom-current-controlled sand deposits - a review of modern shallow- to deep-water environments. Sedimentary Geology 115, 53-80.

Viana, A.R., Faugères, J.-C., Kowsmann, R.O., Lima, R.O., Caddah, J.A.M., Rizzo, J.G., 1998b. Hydrology, morphology and sedimentology of the Campos continental margin, offshore Brazil, in: Stow, D.A.W., Faugères, J.-C. (Eds.), Contourites, Turbidites and Process Interaction. Sedimentary Geology 115, 133-157.

Vorren, T.O., Hald, M., Thomsen, E., 1984. Quaternary sediments and environments on the continental shelf off northern Norway. Marine Geology 57, 229-257.

Vorren, T.O., Lebesbye, E., Andreassen, K., Larsen, K.-B. 1989. Glacigenic sediments on a passive continental margin as exemplified by the Barents Sea. Marine Geology 85, 251-272.

Vorren, T.O., Laberg, J.S., Blaume, F., Dowdeswell, J.A., Kenyon, N.H., Mienert, J., Rumohr, J., Werner, F., 1998. The Norwegian-Greenland Sea continental margins: morphology and late Quaternary sedimentary processes and environment. Quaternary Science Reviews 17, 273-302.

Winsborrow, M.C.M., Andreassen, K., Corner, G.D., Laberg, J.S. 2010. Deglaciation of a marine-based ice sheet: late Weichselian palaeo-ice dynamics and retreat in the southern Barents Sea reconstructed from onshore and offshore glacial geomorphology. Quaternary Science Review 29, 424-442.

Wynn, R.B., Masson, D.G., Stow, D.A.V., Weaver, P.P.E., 2000. Turbidity current sediment waves on the submarine slopes of the western Canary Islands. Marine Geology 163, 185-198.

Wynn, R.B., Stow, D.A.V., 2002. Classification and characterisation of deep-water sediment waves. Marine Geology 192, 7-22.

Figure Captions

Figure 1. Location of the sandwave study area on the southwest Barents Sea continental slope. Red areas mark sandwave fields.

Figure 2. 3-D rendering of multibeam sonar shaded relief bathymetry showing the general setting of the sandwave fields (dark grey, designated N1 to N5 and S1). These are situated below a glaciated and (relict) iceberg scoured shelf, south of the large Bear Island Slide, and superimposed on multiple canyon-like chutes mainly from glacial processes. The bedforms range from 480 to 750 m water depth. Bottom panel is a closer view and low-angle perspective of the S1 field.

Figure 3. Outline of the sandwave fields in the context of the MAREANO surficial geology (genesis) map. Also shown are sample, video, map and seismic illustration locations
.

Figure 4. Topas sub-bottom profiler transect across the S1 sandwave field. The lower panel (C-D) connects with the larger (D-E). Small sandwaves lie on top of stratified glacimarine sediments. See Fig. 3 for location.

Figure 5. Topas sub-bottom profiler longitudinal transect across the N2 sandwave field. GDF-filled channels (e.g. positions a and b, flow tops locally shown in orange) are overlain by a blanket of glacimarine muds about 3 m thick (top shown, yellow). It is locally covered with subsequent GDFs just beneath the sandwaves, their base locally marked in green. See Fig. 3 for location.

Figure 6. Post glacial slide in field N4 showing evacuation and deposition slide elements. Most such failures involve both GDFs and glacimarine deposits. The sandwaves cross the feature, unaffected. See Fig. 3 for location.

Figure 7. Topas sub-bottom profiler transect across the northern area of the S1 field. The relatively steep bedform faces create hyperbolic side-echo artifacts. The base of the sand field is

1085 glacially-derived diamicts and stratified muds. Sand here is 1-4 m thick while bedform amplitude
1086 is about one metre. See Figure 3 for location.
1087
1088 Figure 8. Oceanographic setting at the sandwave fields. Lower left panel shows stylized
1089 components of the North Atlantic Current (NAC), the Norwegian Coastal Current (NCC) and the
1090 Norwegian Atlantic Current (NwAC). Red box blow-up, lower right shows location of a series of
1091 nine CTD casts (April 2011) in relation to the sandwave fields (location in Fig. 3) while the
1092 upper panel shows temperature and salinity from those casts (white vertical lines are the CTD
1093 locations). Note the transition depth between North Atlantic Water (NAW) and Norwegian Sea
1094 Arctic Intermediate Water (NSAIW).
1095
1096 Figure 9. Bathymetric profile of sandwaves in the N1 field demonstrating derivation of the
1097 metrics. Profiles generated normal to the sandwaves at 100 m spacing (red) were smoothed
1098 (blue). Crest and trough elevations and coordinates were auto-picked and further attributed with
1099 a variety of morphometric parameters.
1100
1101 Figure 10. Shade relief showing spreadsheet-derived auto-pick results for recognition of bedform
1102 troughs (red) and crests (green). Vertical lines mark the auto-pick generated points on the profile
1103 panel and the corresponding pick locations on the shaded relief map (in GIS). Open horizontal
1104 arrows (lower panel) highlight large forms not recognized with the auto-pick. The trough sites
1105 were assigned the morphometric attributes noted in Fig. 9.
1106
1107 Figure 11. Shaded relief multibeam echosounder image (illumination from NW) showing pattern
1108 of sandwave crestline traces for the N1 field (white bathymetric contours in metres). Inserts A
1109 and B show details without traces. Double arrows align with flow-parallel elements marking
1110 subtle discontinuities in the crestlines in insert B. Insert C shows acoustic backscatter strength
1111 over the shaded relief image (darker is higher backscatter; more gravelly). See Fig. 3 for
1112 location.
1113
1114 Figure 12. Rose plot of the crestline orientations of many of the sandwaves (black) in relation to
1115 the general bathymetric contours (grey). Transect profile orientations for the measured sandwave

fields and sub-fields (a to e) shown as dashed lines. Crestline trace measurements are for each 150 m long segment of a manual trace of the crest. Similar segmentation applies for the bathymetric contours. Number of segment measurements in italics. Orientations are strongly constrained to attitudes normal to the contours, consistent with contour current-driven bedforms.

Figure 13. Photographic stills from video transects across the sandwaves (10 cm between red lasers). Crests highlighted in lower left. Locations of R-stations, Fig. 3.

Figure 14. Summary of basic bedform metrics for individual sandwave fields. Vertical lines are one sigma.

Figure 15. Frequency distribution of sandwave water depths (a), heights (b) and wavelengths (c) for all fields.

Figure 16. Height versus wavelength plot (a) of all sandwaves in a context of activity level equations by Flemming (1980), H/L ratio frequency distribution (b), and comparison among fields of proportion of sandwaves deemed active by these criteria (c).

Figure 17. Distribution of symmetry measurements for all fields (a). The heavy black line marks symmetric forms. Comparison of the slope value distribution for NW (lee) and SE (stoss) flanks (b). Distributions slightly favor a NW skew and a greater NW slope value, especially in the steeper (5 to 10^{o}) range.

Figure 18. Symmetry of bedforms in the N1 sandwave field superimposed on shaded relief bathymetry (a). Arrows demarcate thalwegs of GDF chutes. The colour banding across the field follows the chutes. The sandwave symmetry is tuned to the GDF chute flanks (b) with an up-hill skew on opposite flanks, the NW flank examples apparently migrating against the main current.

Figure 19. Symmetry distributions of N1 field sandwaves for five height classes. Note the separation of base levels (zero occurrences) to minimize curve overlap.

Figure 20. Paths of maximum slope from selected crestline points. Three paths are highlighted with bathymetric profiles (insert). Most paths show an abrupt directional change at the base of the sandwave (trough), generally matching an inflection point in the corresponding profile. Below the inflection the regional slope is about 1°. A periodic up-slope sand transport is inferred to counter cumulative downslope drift and help maintain sand in the field.

Table Captions

Table 1. Summary of sandwave field dimensions, height and wavelengths and symmetry derived from multibeam sonar bathymetric grid.

Table 2. Summary of sandwave slope metrics, backscatter and sand source and sink estimates.

Figure 1

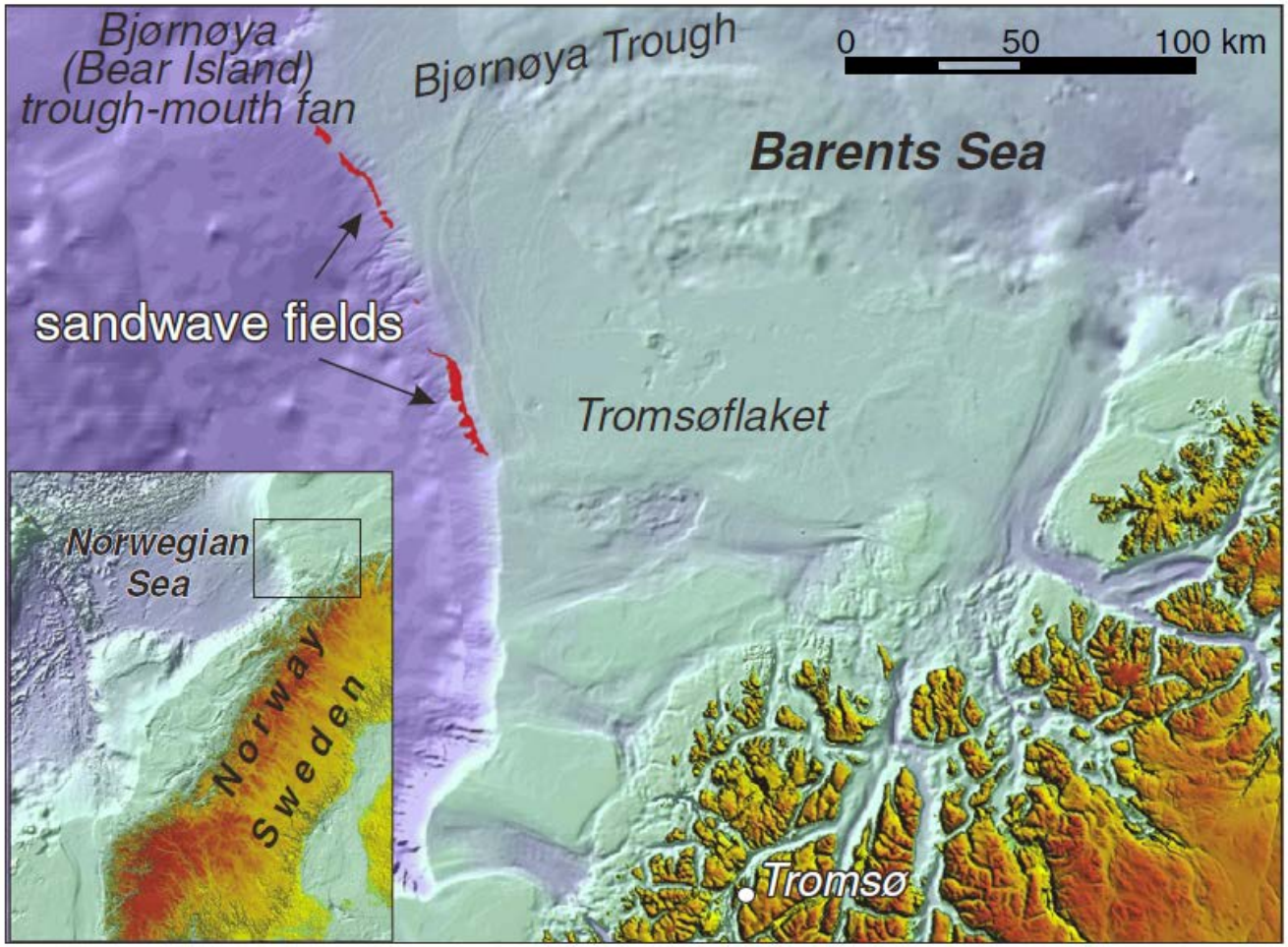
Bjørnøya
(Bear Island)
trough-mouth fan
Bjørnøya Trough
0
50
100 km
Barents Sea
sandwave fields
Tromsøflaket
Norwegian
Sea
Norway
Sweden
Tromsø

Figure 2

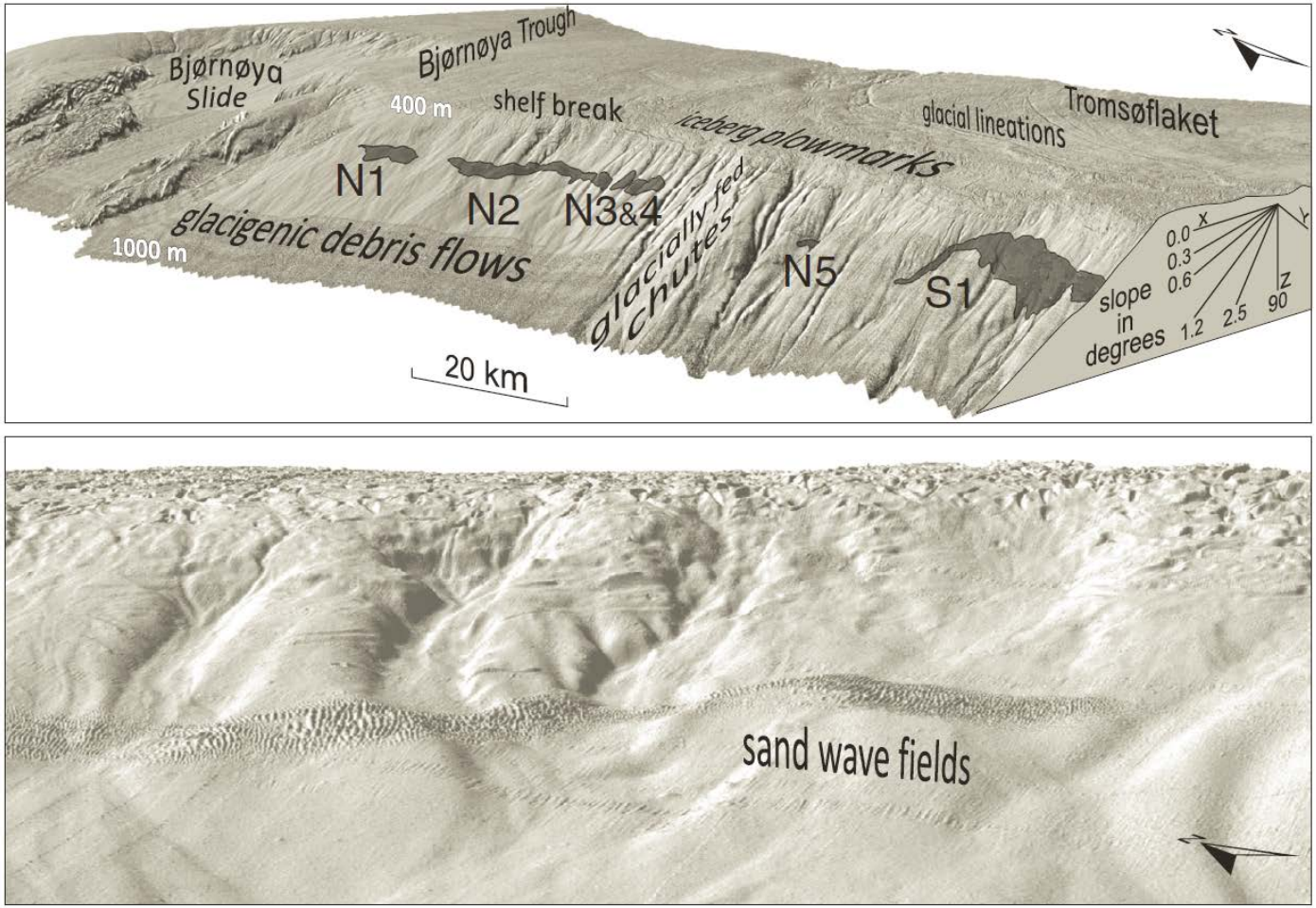
Bjørnøya Slide
Bjørnøya Trough
400 m
shelf break
iceberg plowmarks
glacial lineations
Tromsøflaket
N1
N2
N3&4
glacigenic debris flows
1000 m
glacially fed chutes
N5
S1
20 km
slope in degrees
0.0
0.3
0.6
1.2
2.5
90
x
y
z
sand wave fields

Figure 3

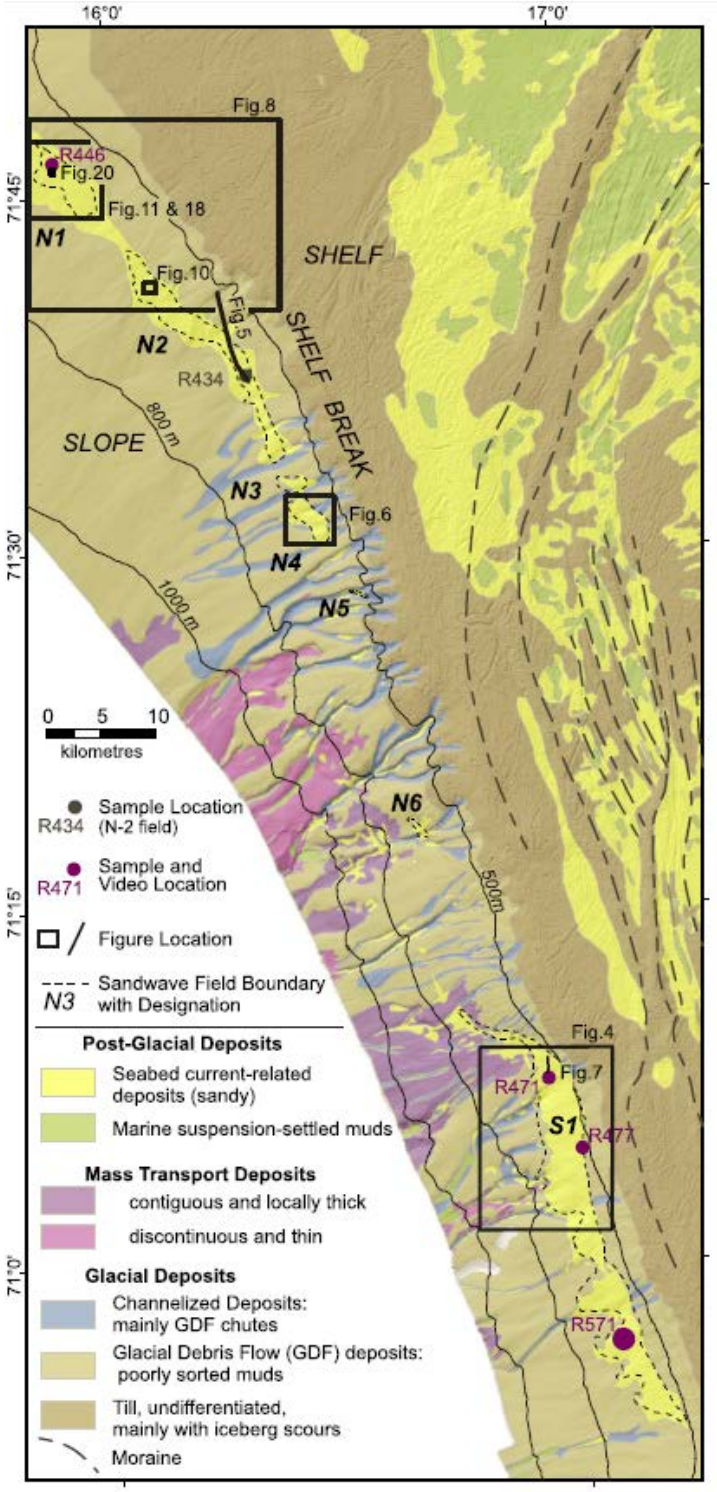
16°0'
17°0'
71°45'
71°30'
71°15'
71°0'
Fig.8
R446
Fig.20
Fig.11 & 18
N1
Fig.10
Fig.5
SHELF
SHELF BREAK
N2
R434
SLOPE
800 m
N3
Fig.6
N4
N5
1000 m
N6
500m
Fig.4
Fig.7
R471
S1
R471
R571
0 5 10
kilometres
Sample Location
R434 (N-2 field)
Sample and
R471 Video Location
Figure Location
Sandwave Field Boundary
N3 with Designation
Post-Glacial Deposits
Seabed current-related deposits (sandy)
Marine suspension-settled muds
Mass Transport Deposits
contiguous and locally thick
discontinuous and thin
Glacial Deposits
Channelized Deposits: mainly GDF chutes
Glacial Debris Flow (GDF) deposits: poorly sorted muds
Till, undifferentiated, mainly with iceberg scours
Moraine

Figure 4

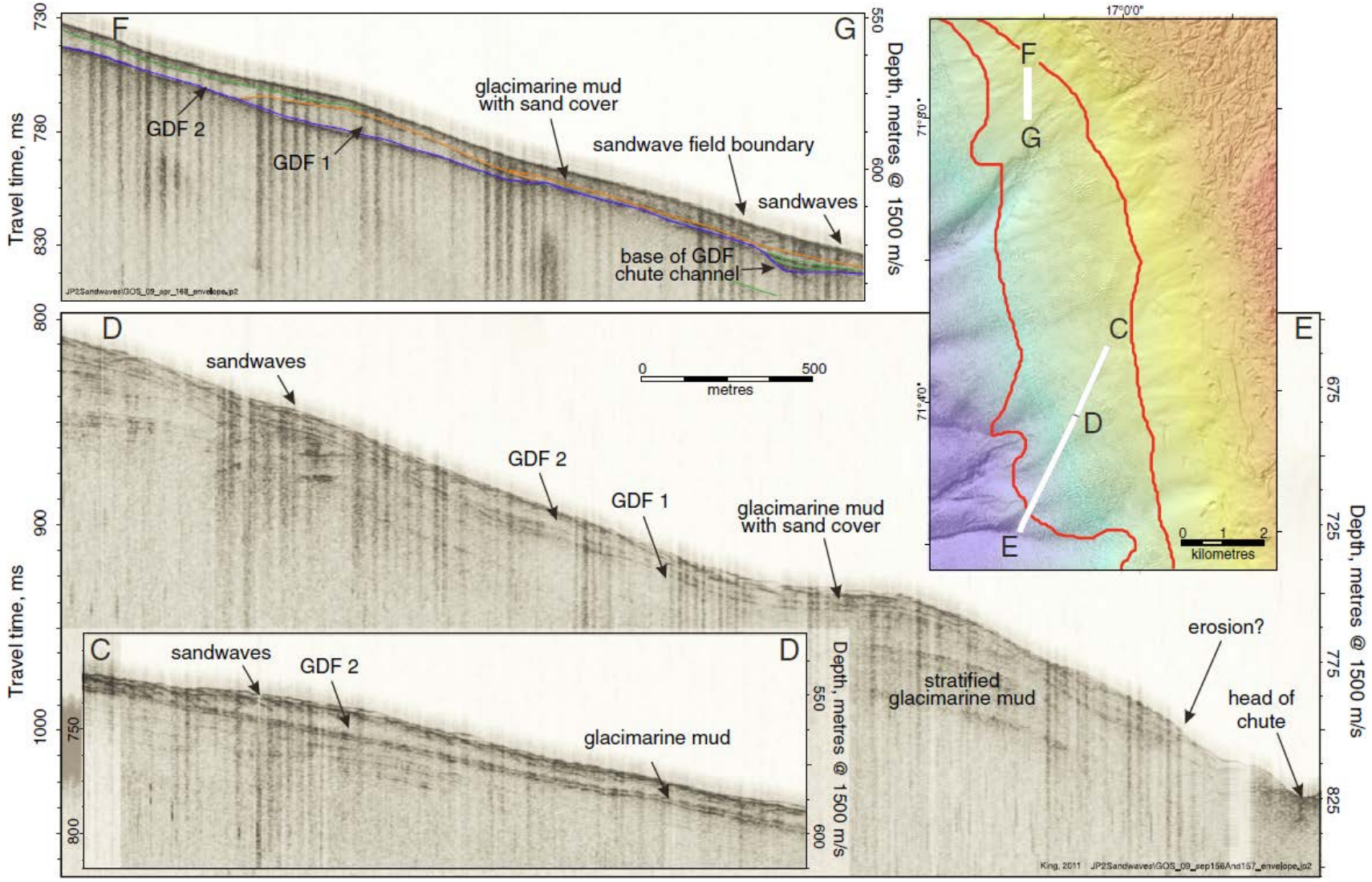
F
G
GDF 2
GDF 1
glacimarine mud
with sand cover
sandwave field boundary
sandwaves
base of GDF
chute channel
Travel time, ms
Depth, metres @ 1500 m/s
730
780
830
550
600
JP2Sandwaves\GOS_09_apr_168_envelope.jp2
D
sandwaves
GDF 2
GDF 1
glacimarine mud
with sand cover
0
500
metres
800
900
1000
675
725
775
825
C
sandwaves
GDF 2
glacimarine mud
750
800
erosion?
stratified
glacimarine mud
head of
chute
King, 2011 JP2Sandwaves\GOS_09_sep156A_rd157_envelope.jp2
17°0'0"
71°8'0"
71°4'0"
E
0
1
2
kilometres

Figure 5

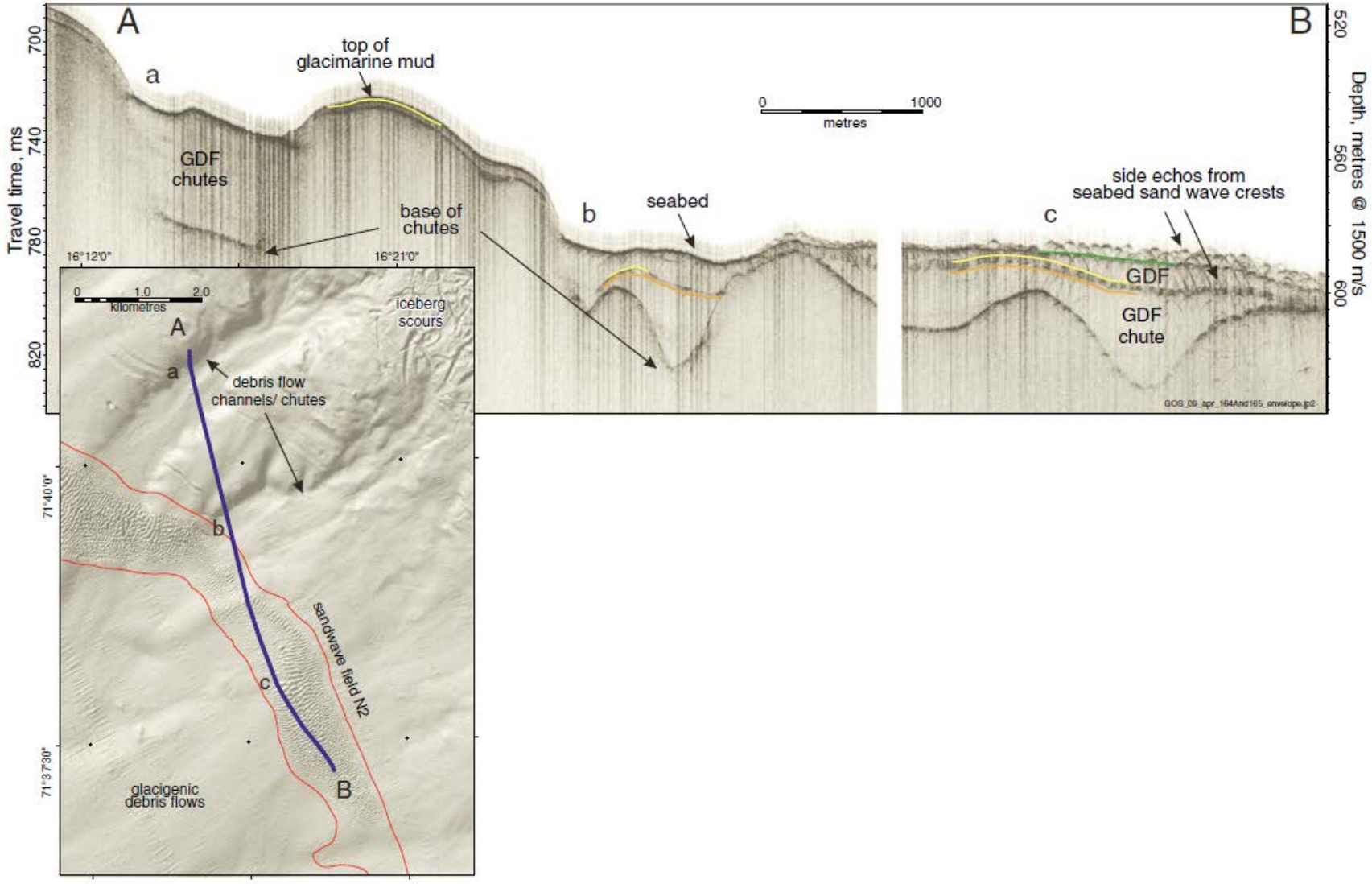
A
B
a
b
c
top of glacimarine mud
GDF chutes
base of chutes
seabed
side echos from seabed sand wave crests
GDF
GDF chute
0
1000
metres
Travel time, ms
700
740
780
820
520
560
600
Depth, metres @ 1500 m/s
16°12'0"
16°21'0"
0
1.0
2.0
kilometres
iceberg scours
debris flow channels/ chutes
sandwave field N2
glacigenic debris flows
71°40'0"
71°37'30"

Figure 6

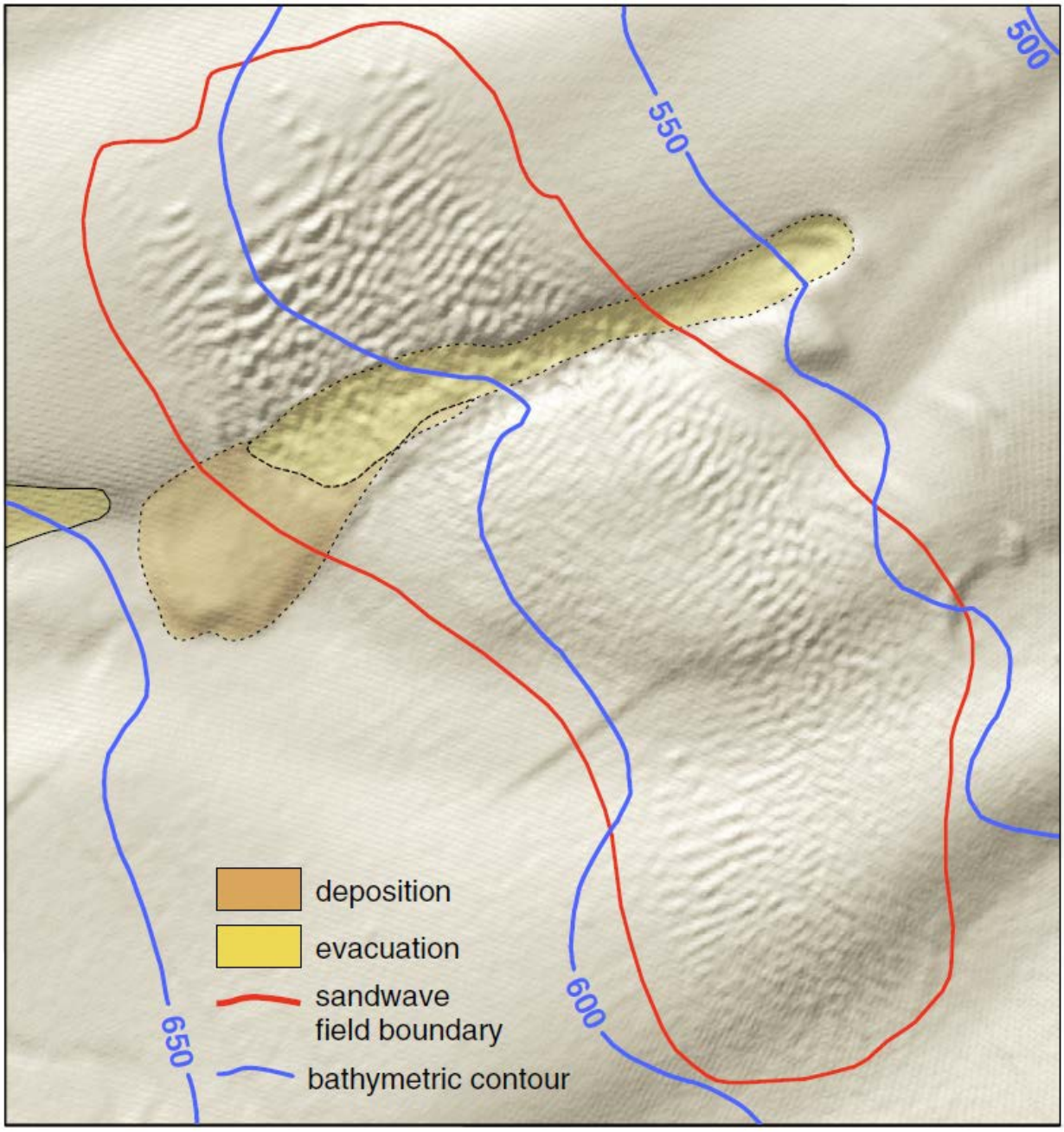
500
550
600
650
deposition
evacuation
sandwave
field boundary
bathymetric contour

Figure 7

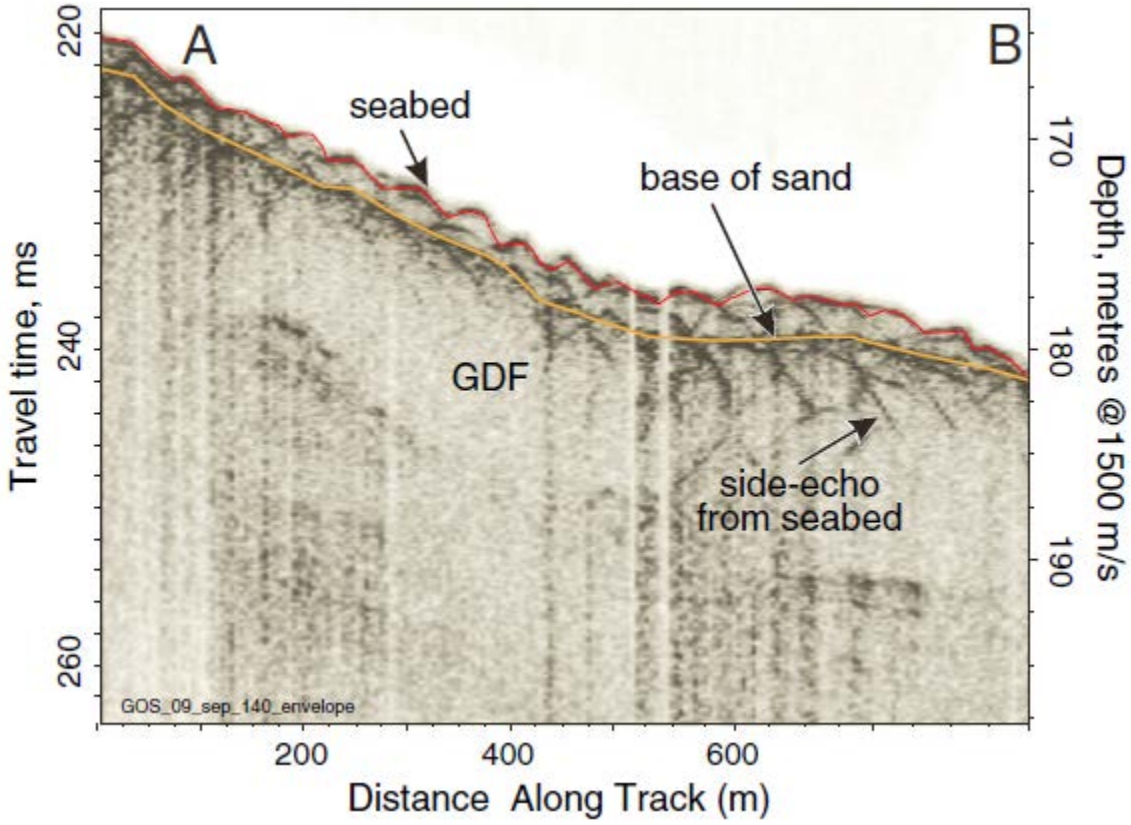
A
B
seabed
base of sand
GDF
side-echo
from seabed
GOS_09_sep_140_envelope
Travel time, ms
220
240
260
Depth, metres @1500 m/s
170
180
190
200
400
600
Distance Along Track (m)

Figure 8

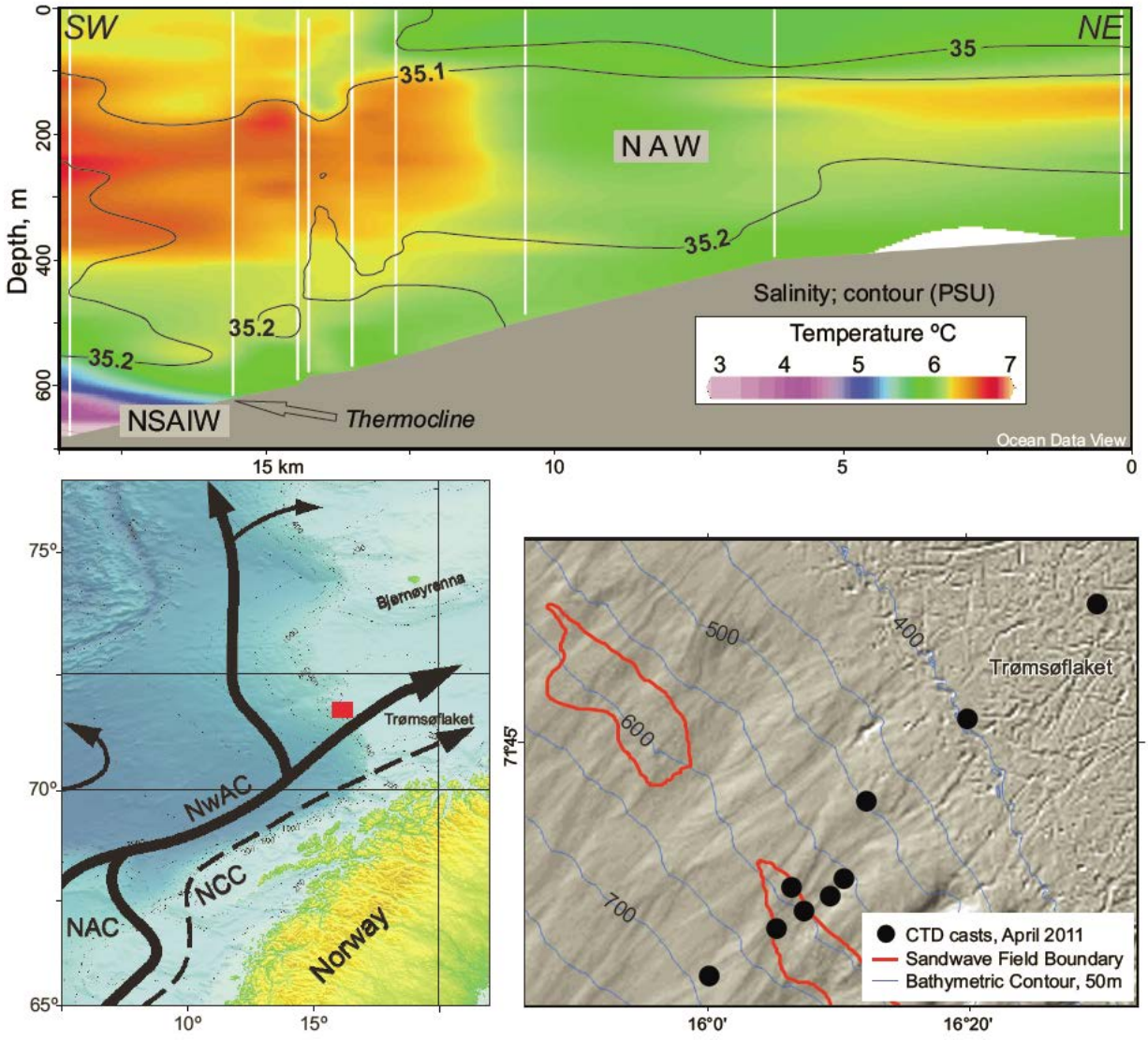
SW
NE
35
35.1
NAW
35.2
35.2
35.2
Salinity; contour (PSU)
Temperature ºC
3 4 5 6 7
NSAIW
Thermocline
Ocean Data View
Depth, m
0
200
400
600
15 km
10
5
0
75º
70º
65º
10º
15º
Bjørnøyrenna
Trømsøflaket
NwAC
NCC
NAC
Norway
71°45'
500
400
600
700
Trømsøflaket
CTD casts, April 2011
Sandwave Field Boundary
Bathymetric Contour, 50m
16°0'
16°20'

Figure 9

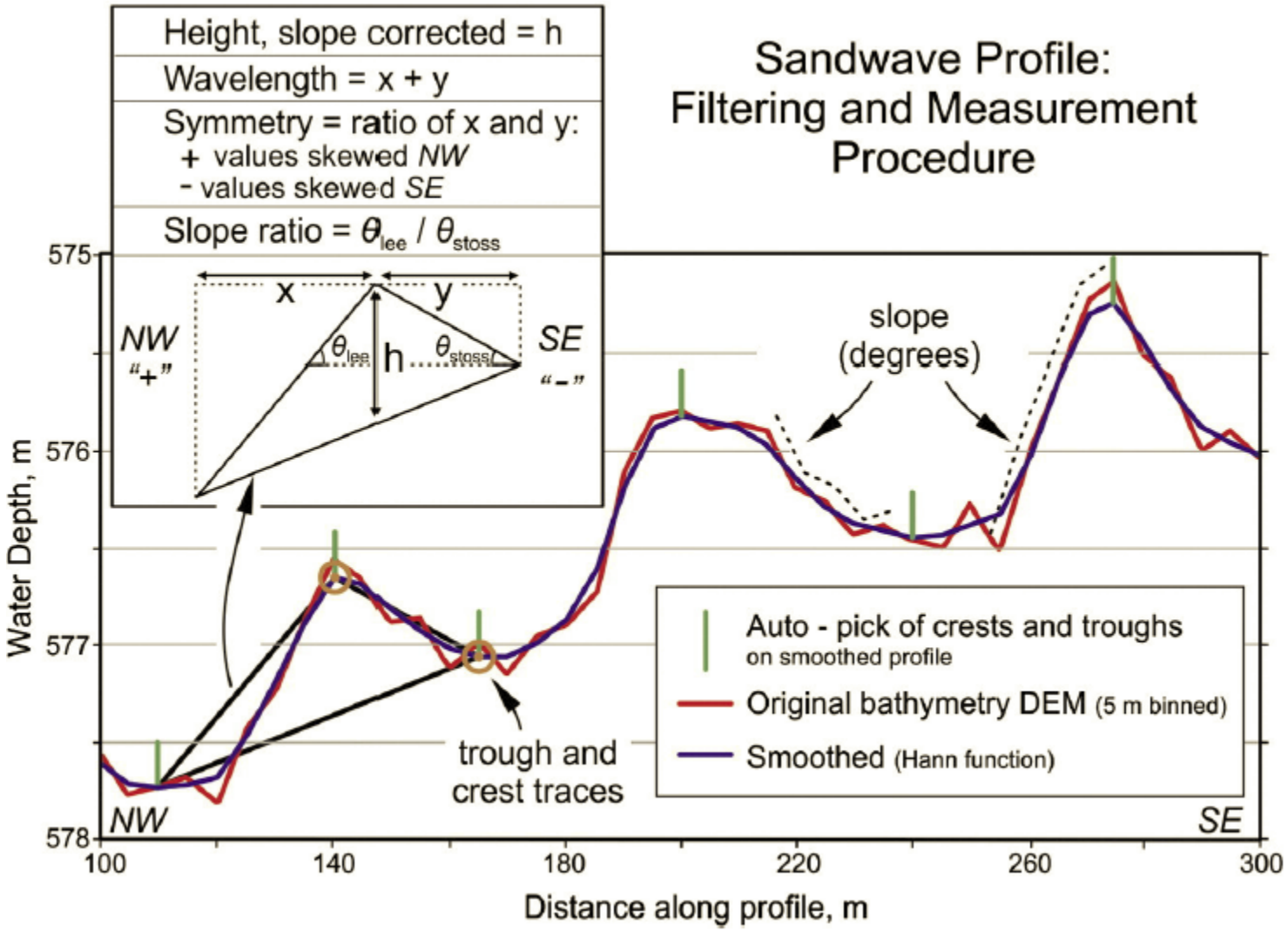
Sandwave Profile:
Filtering and Measurement Procedure
Height, slope corrected = h
Wavelength = x + y
Symmetry = ratio of x and y:
+ values skewed NW
- values skewed SE
Slope ratio = θlee / θstoss
x
y
h
θlee
θstoss
NW
"+"
SE
"-"
slope
(degrees)
Auto - pick of crests and troughs
on smoothed profile
Original bathymetry DEM (5 m binned)
Smoothed (Hann function)
trough and
crest traces
NW
SE
Water Depth, m
575
576
577
578
100
140
180
220
260
300
Distance along profile, m

Figure 10

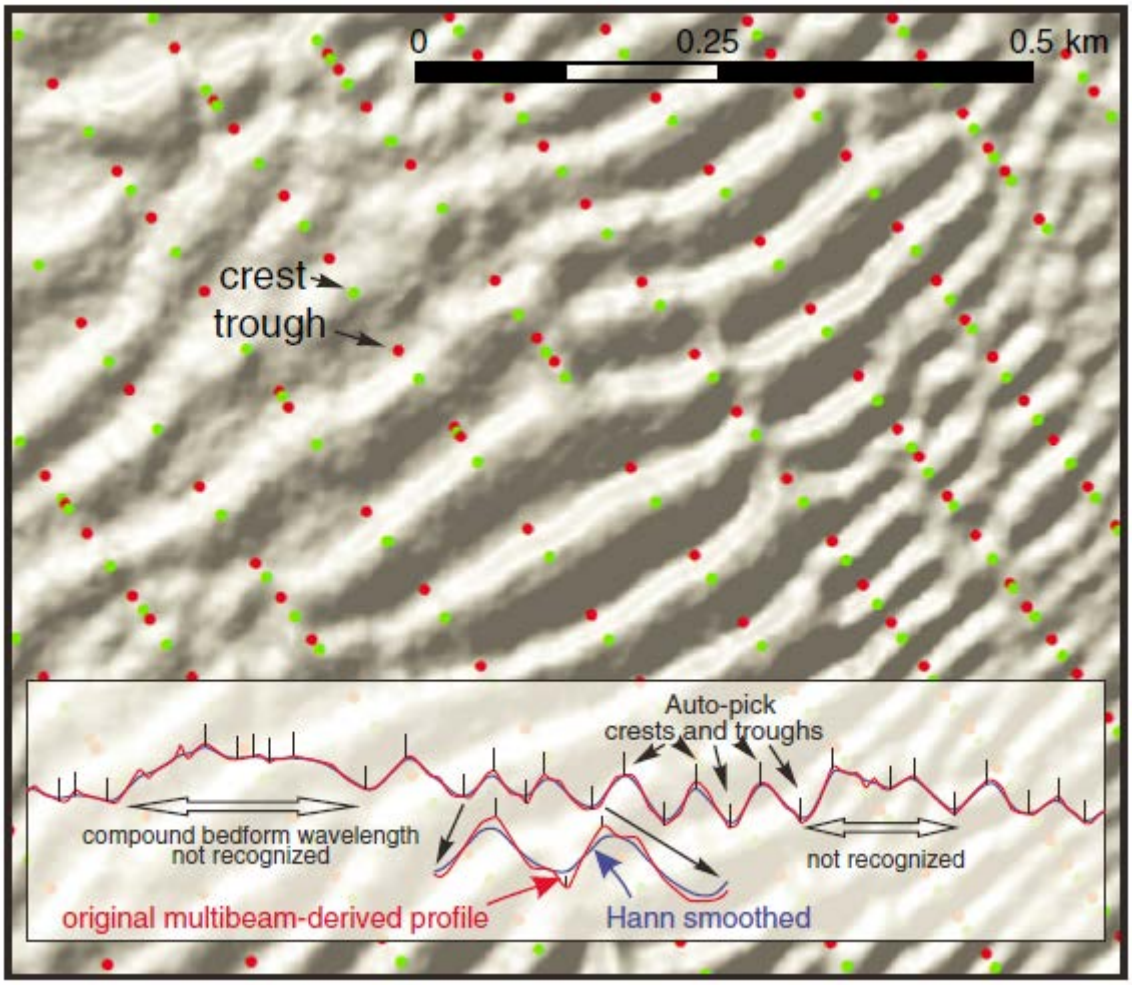
0
0.25
0.5 km
crest
trough
Auto-pick
crests and troughs
compound bedform wavelength
not recognized
not recognized
original multibeam-derived profile
Hann smoothed

Figure 11

Figure 12

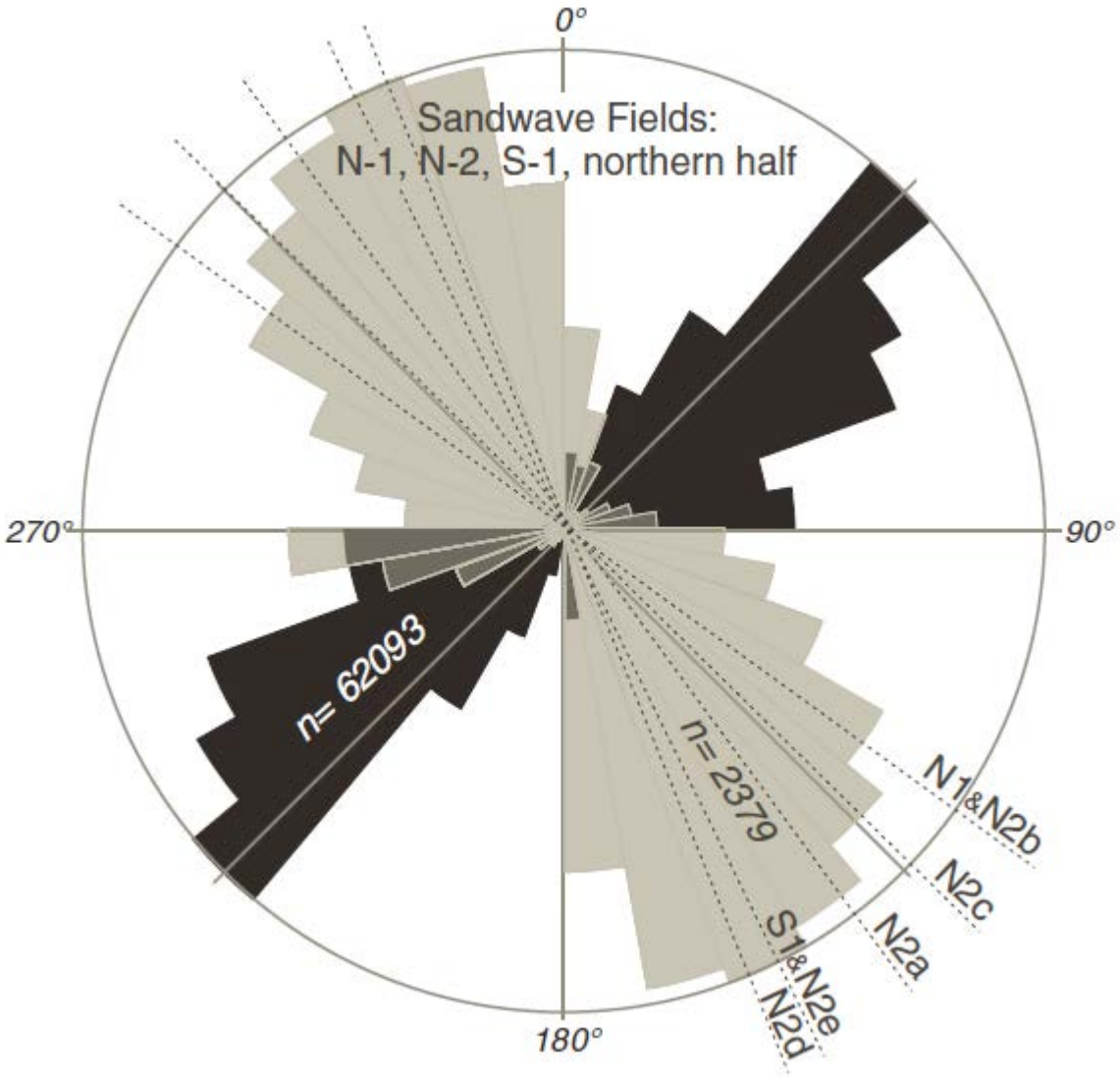
0°
Sandwave Fields:
N-1, N-2, S-1, northern half
270°
90°
180°
n= 62093
n= 2379
N1&N2b
N2c
N2a
S1&N2e
N2d

Figure 13

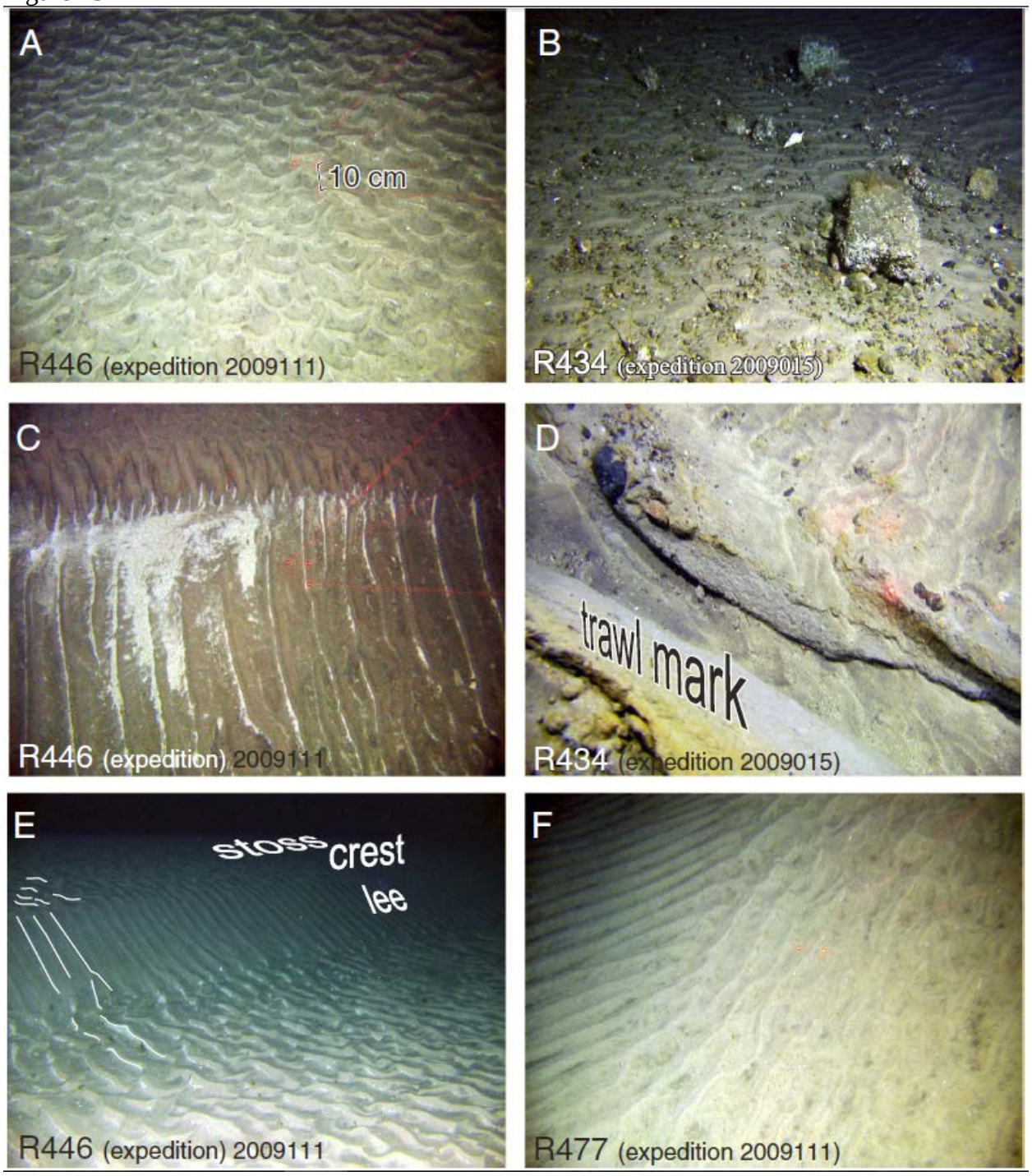
A
10 cm
R446 (expedition 2009111)
B
R434 (expedition 2009015)
C
R446 (expedition) 2009111
D
trawl mark
R434 (expedition 2009015)
E
stoss
crest
lee
R446 (expedition) 2009111
F
R477 (expedition 2009111)

Figure 14

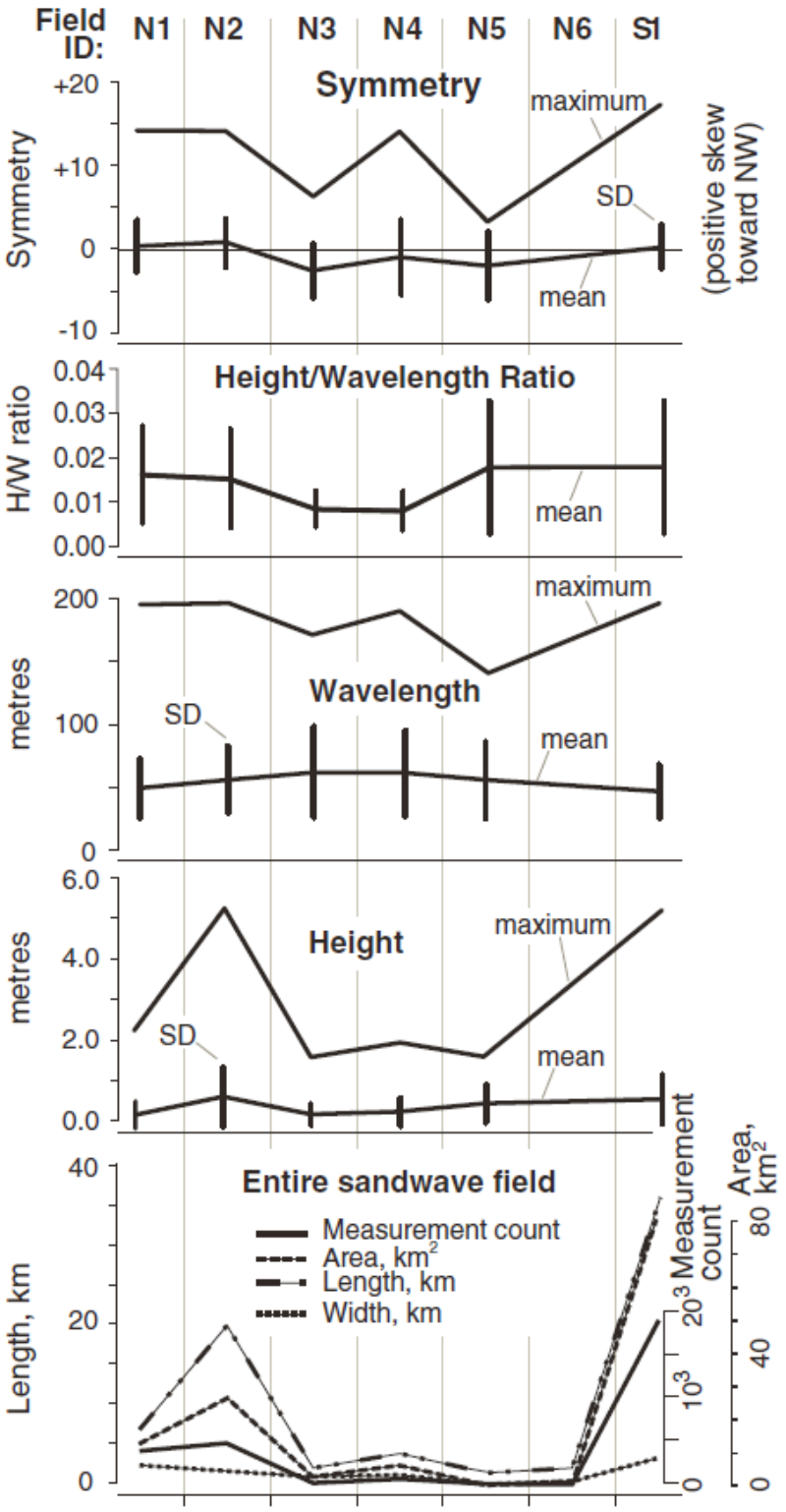
Field ID:
N1
N2
N3
N4
N5
N6
S1
Symmetry
maximum
SD
mean
(positive skew toward NW)
Symmetry
+20
+10
0
-10
Height/Wavelength Ratio
H/W ratio
0.04
0.03
0.02
0.01
0.00
Wavelength
metres
200
100
0
Height
6.0
4.0
2.0
0.0
Entire sandwave field
Measurement count
Area, km2
Length, km
Width, km
Length, km
40
20
0
Measurement count
Area, km2
80
40
0

Figure 15

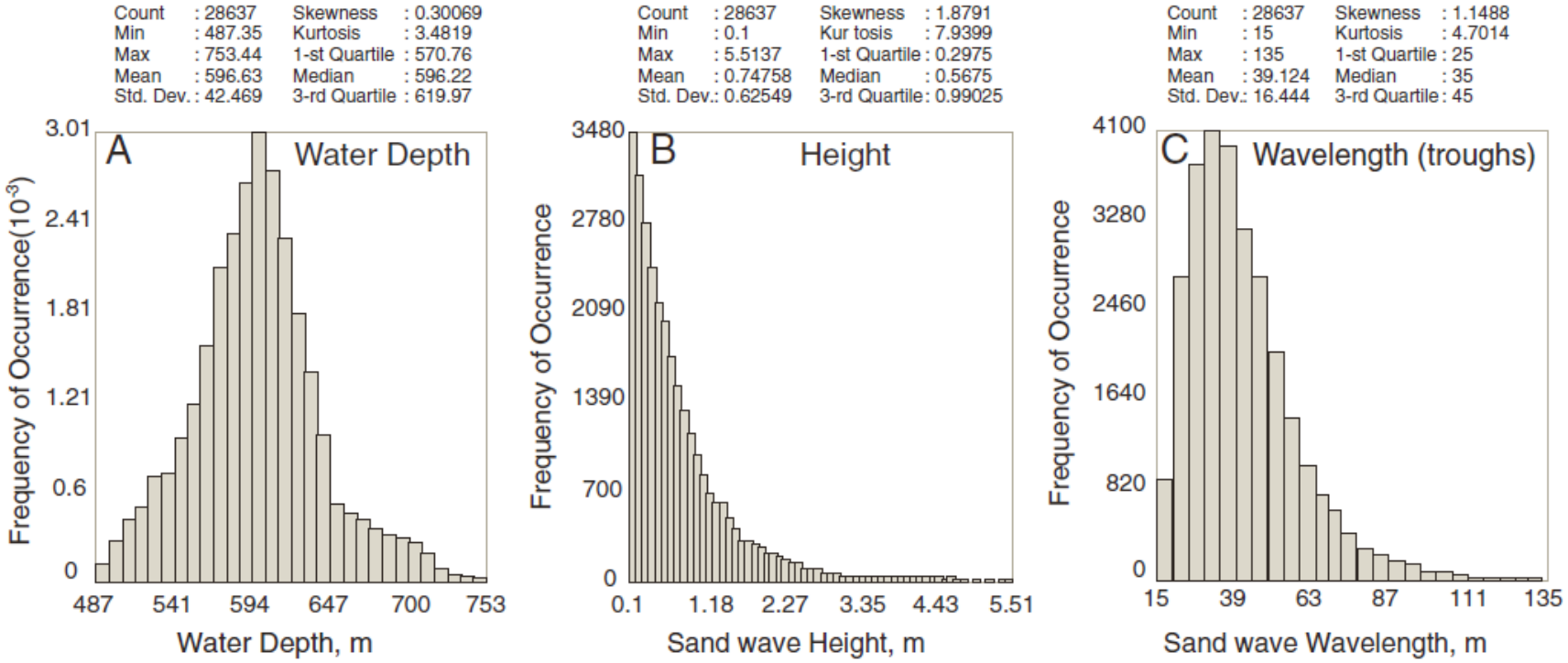
Count : 28637
Min : 487.35
Max : 753.44
Mean : 596.63
Std. Dev. : 42.469
Skewness : 0.30069
Kurtosis : 3.4819
1-st Quartile : 570.76
Median : 596.22
3-rd Quartile : 619.97
A
Water Depth
Frequency of Occurrence(10-3)
3.01
2.41
1.81
1.21
0.6
0
487
541
594
647
700
753
Water Depth, m
Count : 28637
Min : 0.1
Max : 5.5137
Mean : 0.74758
Std. Dev.: 0.62549
Skewness : 1.8791
Kur tosis : 7.9399
1-st Quartile : 0.2975
Median : 0.5675
3-rd Quartile : 0.99025
B
Height
Frequency of Occurrence
3480
2780
2090
1390
700
0
0.1
1.18
2.27
3.35
4.43
5.51
Sand wave Height, m
Count : 28637
Min : 15
Max : 135
Mean : 39.124
Std. Dev.: 16.444
Skewness : 1.1488
Kurtosis : 4.7014
1-st Quartile : 25
Median : 35
3-rd Quartile : 45
C
Wavelength (troughs)
Frequency of Occurrence
4100
3280
2460
1640
820
0
15
39
63
87
111
135
Sand wave Wavelength, m

Figure 16

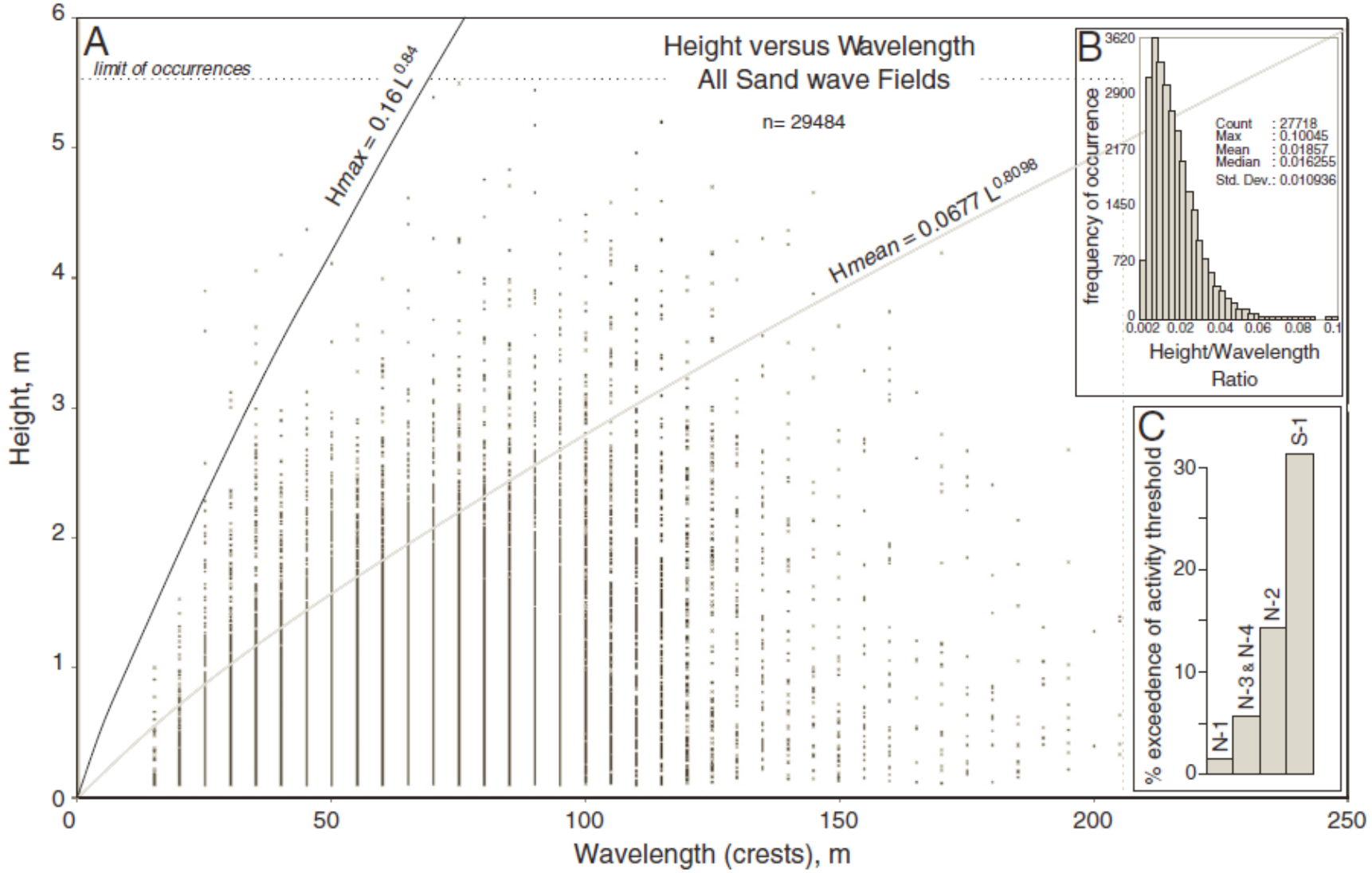
A
limit of occurrences
Hmax = 0.16 L^0.84
Hmean = 0.0677 L^0.8098
Height versus Wavelength
All Sand wave Fields
n= 29484
Height, m
Wavelength (crests), m
0
1
2
3
4
5
6
0
50
100
150
200
250
B
frequency of occurrence
3620
2900
2170
1450
720
0
0.002 0.02 0.04 0.06 0.08 0.1
Height/Wavelength
Ratio
Count : 27718
Max : 0.10045
Mean : 0.01857
Median : 0.016255
Std. Dev.: 0.010936
C
% exceedence of activity threshold
30
20
10
0
N-1
N-3 & N-4
N-2
S-1

Figure 17

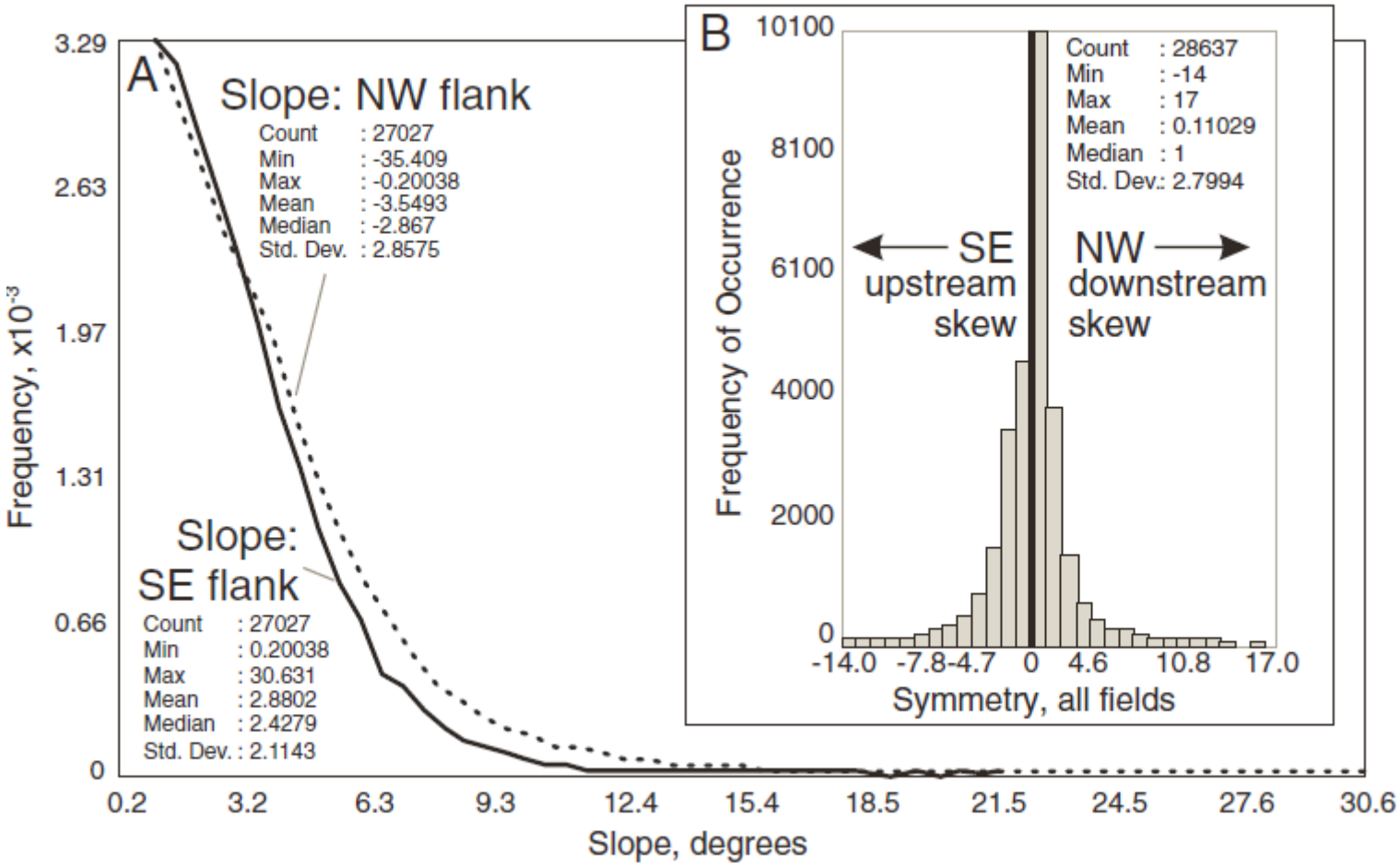
A
Slope: NW flank
Count : 27027
Min : -35.409
Max : -0.20038
Mean : -3.5493
Median : -2.867
Std. Dev. : 2.8575
Slope: SE flank
Count : 27027
Min : 0.20038
Max : 30.631
Mean : 2.8802
Median : 2.4279
Std. Dev. : 2.1143
Frequency, x10-3
3.29
2.63
1.97
1.31
0.66
0
0.2
3.2
6.3
9.3
12.4
15.4
18.5
21.5
24.5
27.6
30.6
Slope, degrees
B
Count : 28637
Min : -14
Max : 17
Mean : 0.11029
Median : 1
Std. Dev.: 2.7994
SE upstream skew
NW downstream skew
Frequency of Occurrence
10100
8100
6100
4000
2000
0
-14.0
-7.8
-4.7
0
4.6
10.8
17.0
Symmetry, all fields

Figure 18

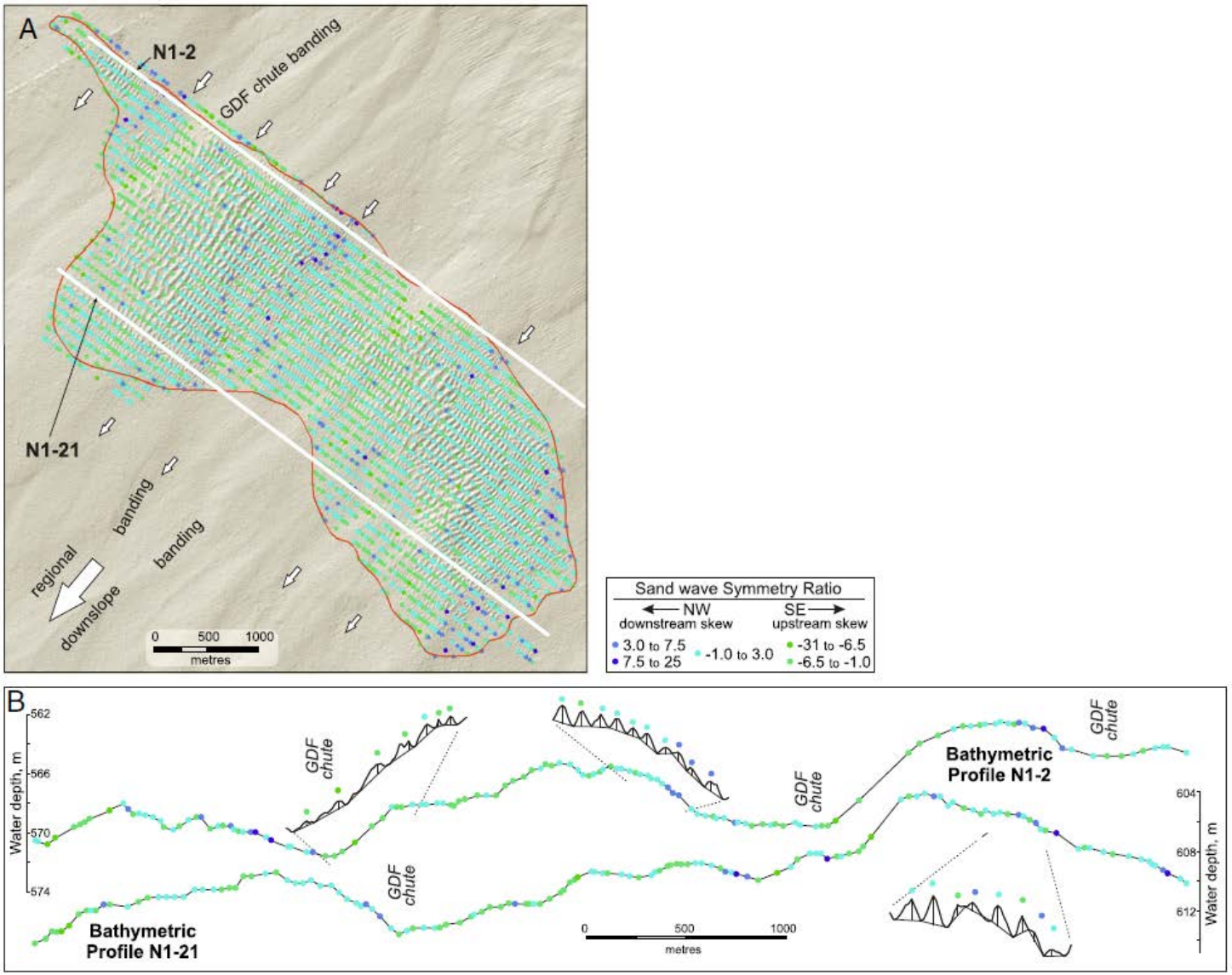
A
N1-2
GDF chute banding
N1-21
banding
banding
regional
downslope
0 500 1000
metres
Sand wave Symmetry Ratio
NW
downstream skew
SE
upstream skew
3.0 to 7.5
7.5 to 25
-1.0 to 3.0
-31 to -6.5
-6.5 to -1.0
B
Water depth, m
562
566
570
574
GDF chute
GDF chute
GDF chute
GDF chute
Bathymetric Profile N1-2
Bathymetric Profile N1-21
0 500 1000
metres
604
608
612
Water depth, m

Figure 19

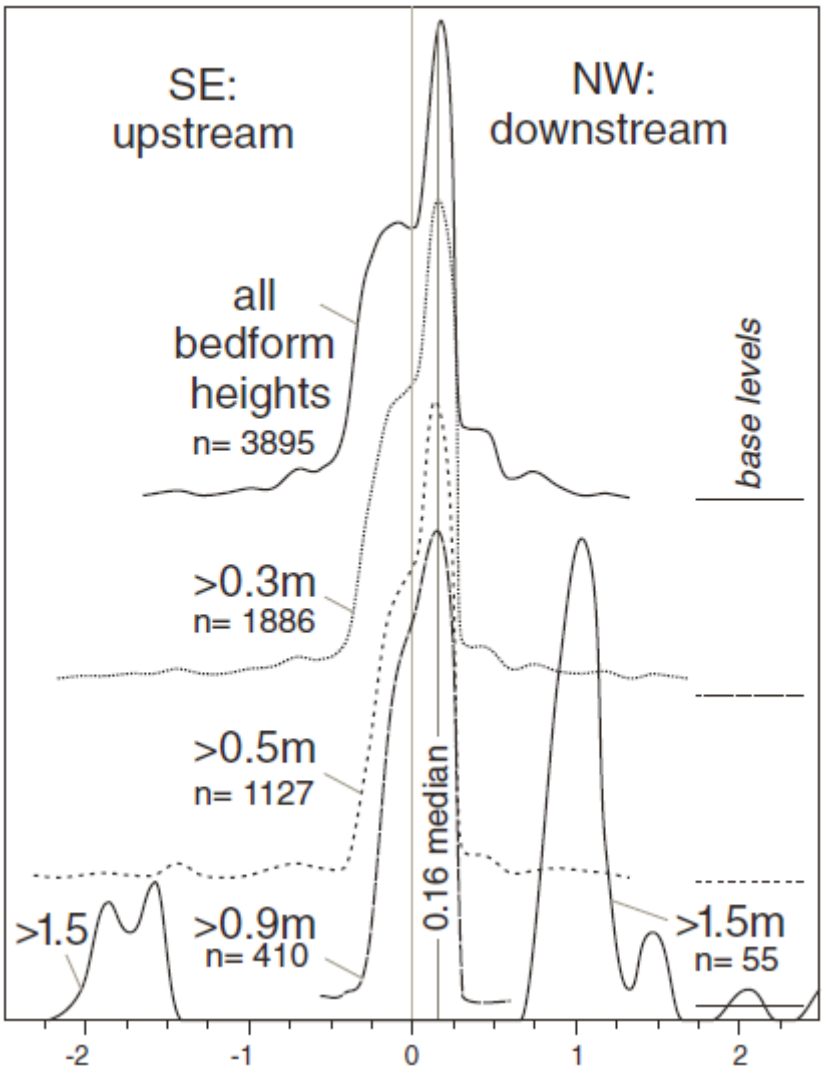
SE:
upstream
NW:
downstream
all
bedform
heights
n= 3895
base levels
>0.3m
n= 1886
>0.5m
n= 1127
0.16 median
>1.5
>0.9m
n= 410
>1.5m
n= 55
-2
-1
0
1
2

Figure 20

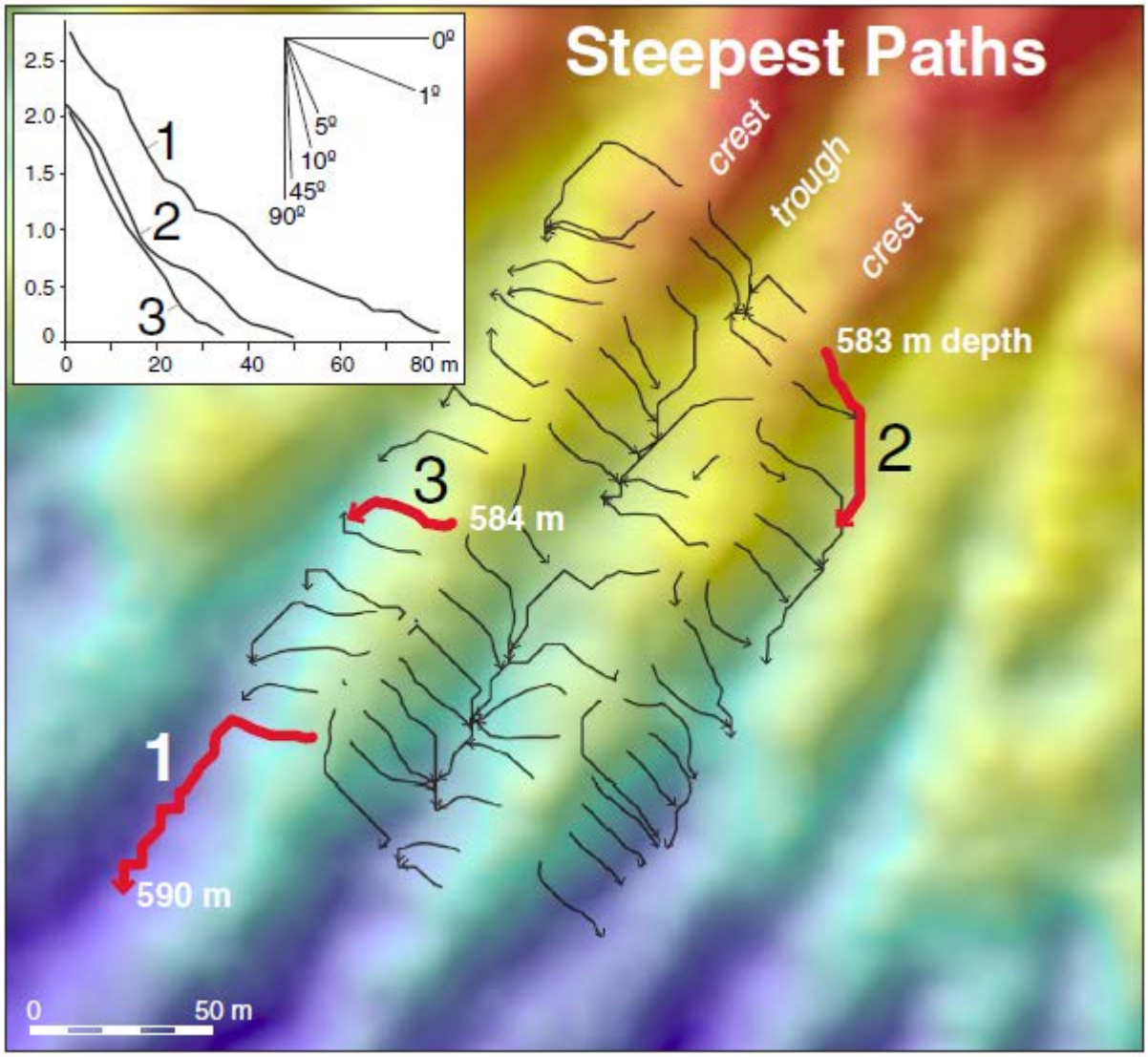
Steepest Paths
crest
trough
crest
583 m depth
2
3
584 m
1
590 m
0
50 m
2.5
2.0
1.5
1.0
0.5
0
0
20
40
60
80 m
0º
1º
5º
10º
45º
90º
1
2
3

Table 1

Summary of sandwave field dimensions, height and wavelengths and symmetry derived from multibeam sonar bathymetric grid.

Field ID	Length	Width	Area	Water depth			No. measurements	Height			Wavelength (crests)				Height wavelength ratio		Symmetry (positive is downstream; NW)			
	km	km	sq. km	Maximum	Minimum	Mean	At 100 m spacing along crest	Maximum	Mean	SD	Maximum	Minimum	Mean	SD	H/W mean	SD	Maximum	Minimum	Mean	SD
N1	7	2.7	12	648	561	600	3840	2.5	0.4	0.3	205	15	58.6	23.8	0.019	0.011	14	−14	0.2	3.1
N2	20.1	1.8	26	564	645	606	4831	5.5	0.9	0.8	205	15	65.3	26.1	0.018	0.011	14	−14	0.6	3.0
N3	2.3	1	2	609	548	581	170	1.9	0.4	0.3	180	20	70.8	36.1	0.011	0.004	6	−12	−2.8	3.3
N4	4.1	1.4	6	623	550	588	567	2.2	0.5	0.4	200	15	71.0	34.9	0.010	0.004	14	−14	−1.1	4.5
N5	1.6	0.17	0	582	553	574	47	1.9	0.7	0.5	150	25	65.3	31.3	0.020	0.015	3	−13	−2.2	4.1
N6	2.2	0.4	1	702	652	671	0	Low amplitude and noisy data							–	–	–	–	–	–
S1	36	3.5	82	753	487	594	19182	5.5	0.8	0.6	205	15	55.8	22.0	0.020	0.015	17	−14	0.0	2.6
All fields	73	11	130	753	487	602	28637	5.5	0.6	0.5	205	15	64.5	29.0	0.016	0.010	17	−14	0.9	3.4

Table 2

Summary of sandwave slope metrics, backscatter and sand source and sink estimates.

Field ID	Slope, NW flank			Slope, SE flank			Slope ratio (negative suggests flow toward NW)				Backscatter strength, dB				Sandwave Field Volume Estimate (10^6 m^3)	Winnowed source thickness estimate: sink volume equivalent at 10:1 reduction of parent diamict through winnowing			
																Source area		Thickness equivalent	
	Maximum	Mean	SD	Maximum	Mean	SD	Minimum	Maximum	Mean	SD	Maximum	Minimum	Mean	SD	From morpho-metrics	Upslope source area only (km^2)	Upslope plus shelf source area (km^2)	Upslope winnowed thickness (cm)	Upslope and shelf winnowed thickness (cm)
N1	9.6	2.0	1.4	6.3	1.8	1.2	−14	16	0.4	2.6	−3	−35	−17.7	4.9	3.9	50.0	300.0	78	13
N2	24.3	3.4	3.1	30.6	2.9	2.1	−31	48	0.2	3.8	−3	−39	−17.4	5.0	15.7	100.0	300.0	157	52
N3	5.5	2.0	1.0	5.9	1.4	1.0	−9	19	1.7	3.6	−6	−37	−19.2	5.2	0.5	5.0	20.0	99	25
N4	6.7	1.9	1.2	5.5	1.4	1.0	−14	16	0.9	4.0	−2	−36	−16.8	5.7	1.4	15.0	40.0	93	35
N5	12.1	2.9	1.9	20.7	4.1	5.1	−12	7	0.1	4.1	−2	−32	−15.0	7.3	0.1	2.0	30.0	47	3
N6	Low amplitude and noisy data					–	–	–	–	–	–	–	–	–	–	10.0	56.0	–	–
S1	35.4	3.9	2.9	21.8	3.0	2.2	−54	77	0.7	3.7	2	−48	−17.8	6.2	50	170	400	295	125
All fields	35.4	2.7	1.9	30.6	2.4	2.1	−54	77	0.6	3.6	2	−48	−17.3	5.7	72	352	1146	–	–